arXiv:1412.1169v1 [astro-ph.HE] 3 Dec 2014

ASTRO-H Space X-ray Observatory White Paper

Young Supernova Remnants

J. P. Hughes (Rutgers University), S. Safi-Harb (University of Manitoba),
A. Bamba (Aoyama Gakuin University), S. Katsuda (JAXA), M. Leutenegger (NASA/GSFC),
K. S. Long (STScI), Y. Maeda (JAXA), K. Mori (Miyazaki University), H. Nakajima (Osaka University),
M. Sawada (Aoyama Gakuin University), T. Tanaka (Kyoto University), H. Uchida (Kyoto University),
H. Yamaguchi (NASA/GSFC & UMD), F. Aharonian (DIAS & MPI-K), S. Funk (Stanford University),
J. Hiraga (University of Tokyo), M. Ishida (JAXA), K. Koyama (Kyoto University),
H. Matsumoto (Nagoya University), M. Nobukawa (Kyoto University), M. Ozaki (JAXA),
T. Tamagawa (RIKEN), H. Tsunemi (Osaka University), H. Tomida (JAXA),
Y. Uchiyama (Rikkyo University), and S. Uno (Nihon Fukushi University)
on behalf of the ASTRO-H Science Working Group

Abstract

Thanks to the unprecedented spectral resolution and sensitivity of the Soft X-ray Spectrometer (SXS) to soft thermal X-ray emission, *ASTRO-H* will open a new discovery window for understanding young, ejecta-dominated, supernova remnants (SNRs). In particular we study how *ASTRO-H* observations will address, comprehensively, three key topics in SNR research: (1) using abundance measurements to unveil SNR progenitors, (2) using spatial and velocity distribution of the ejecta to understand supernova explosion mechanisms, (3) revealing the link between the thermal plasma state of SNRs and the efficiency of their particle acceleration.

Complete list of the ASTRO-H Science Working Group

Tadayuki Takahashi[a], Kazuhisa Mitsuda[a], Richard Kelley[b], Felix Aharonian[c], Hiroki Akamatsu[d], Fumie Akimoto[e], Steve Allen[f], Naohisa Anabuki[g], Lorella Angelini[b], Keith Arnaud[h], Marc Audard[i], Hisamitsu Awaki[j], Aya Bamba[k], Marshall Bautz[l], Roger Blandford[f], Laura Brenneman[b], Greg Brown[m], Edward Cackett[n], Maria Chernyakova[c], Meng Chiao[b], Paolo Coppi[o], Elisa Costantini[d], Jelle de Plaa[d], Jan-Willem den Herder[d], Chris Done[p], Tadayasu Dotani[a], Ken Ebisawa[a], Megan Eckart[b], Teruaki Enoto[q], Yuichiro Ezoe[r], Andrew Fabian[n], Carlo Ferrigno[i], Adam Foster[s], Ryuichi Fujimoto[t], Yasushi Fukazawa[u], Stefan Funk[f], Akihiro Furuzawa[e], Massimiliano Galeazzi[v], Luigi Gallo[w], Poshak Gandhi[p], Matteo Guainazzi[x], Yoshito Haba[y], Kenji Hamaguchi[h], Isamu Hatsukade[z], Takayuki Hayashi[a], Katsuhiro Hayashi[a], Kiyoshi Hayashida[g], Junko Hiraga[aa], Ann Hornschemeier[b], Akio Hoshino[ab], John Hughes[ac], Una Hwang[ad], Ryo Iizuka[a], Yoshiyuki Inoue[a], Hajime Inoue[a], Kazunori Ishibashi[e], Manabu Ishida[a], Kumi Ishikawa[q], Yoshitaka Ishisaki[r], Masayuki Ito[ae], Naoko Iyomoto[af], Jelle Kaastra[d], Timothy Kallman[b], Tuneyoshi Kamae[f], Jun Kataoka[ag], Satoru Katsuda[a], Junichiro Katsuta[u], Madoka Kawaharada[a], Nobuyuki Kawai[ah], Dmitry Khangulyan[a], Caroline Kilbourne[b], Masashi Kimura[ai], Shunji Kitamoto[ab], Tetsu Kitayama[aj], Takayoshi Kohmura[ak], Motohide Kokubun[a], Saori Konami[r], Katsuji Koyama[al], Hans Krimm[b], Aya Kubota[am], Hideyo Kunieda[e], Stephanie LaMassa[o], Philippe Laurent[an], François Lebrun[an], Maurice Leutenegger[b], Olivier Limousin[an], Michael Loewenstein[b], Knox Long[ao], David Lumb[ap], Grzegorz Madejski[f], Yoshitomo Maeda[a], Kazuo Makishima[aa], Maxim Markevitch[b], Hironori Matsumoto[e], Kyoko Matsushita[aq], Dan McCammon[ar], Brian McNamara[as], Jon Miller[at], Eric Miller[l], Shin Mineshige[au], Ikuyuki Mitsuishi[e], Takuya Miyazawa[e], Tsunefumi Mizuno[u], Koji Mori[z], Hideyuki Mori[e], Koji Mukai[b], Hiroshi Murakami[av], Toshio Murakami[t], Richard Mushotzky[h], Ryo Nagino[g], Takao Nakagawa[a], Hiroshi Nakajima[g], Takeshi Nakamori[aw], Shinya Nakashima[a], Kazuhiro Nakazawa[aa], Masayoshi Nobukawa[al], Hirofumi Noda[q], Masaharu Nomachi[ax], Steve O' Dell[ay], Hirokazu Odaka[a], Takaya Ohashi[r], Masanori Ohno[u], Takashi Okajima[b], Naomi Ota[az], Masanobu Ozaki[a], Frits Paerels[ba], Stéphane Paltani[i], Arvind Parmar[x], Robert Petre[b], Ciro Pinto[n], Martin Pohl[i], F. Scott Porter[b], Katja Pottschmidt[b], Brian Ramsey[ay], Rubens Reis[at], Christopher Reynolds[h], Claudio Ricci[au], Helen Russell[n], Samar Safi-Harb[bb], Shinya Saito[a], Hiroaki Sameshima[a], Goro Sato[ag], Kosuke Sato[aq], Rie Sato[a], Makoto Sawada[k], Peter Serlemitsos[b], Hiromi Seta[bc], Aurora Simionescu[a], Randall Smith[s], Yang Soong[b], Łukasz Stawarz[a], Yasuharu Sugawara[bd], Satoshi Sugita[j], Andrew Szymkowiak[o], Hiroyasu Tajima[e], Hiromitsu Takahashi[u], Hiroaki Takahashi[g], Yoh Takei[a], Toru Tamagawa[q], Takayuki Tamura[a], Keisuke Tamura[e], Takaaki Tanaka[al], Yasuo Tanaka[a], Yasuyuki Tanaka[u], Makoto Tashiro[bc], Yuzuru Tawara[e], Yukikatsu Terada[bc], Yuichi Terashima[j], Francesco Tombesi[b], Hiroshi Tomida[ai], Yohko Tsuboi[bd], Masahiro Tsujimoto[a], Hiroshi Tsunemi[g], Takeshi Tsuru[al], Hiroyuki Uchida[al], Yasunobu Uchiyama[ab], Hideki Uchiyama[be], Yoshihiro Ueda[au], Shutaro Ueda[g], Shiro Ueno[ai], Shinichiro Uno[bf], Meg Urry[o], Eugenio Ursino[v], Cor de Vries[d], Shin Watanabe[a], Norbert Werner[f], Dan Wilkins[w], Shinya Yamada[r], Hiroya Yamaguchi[b], Kazutaka Yamaoka[e], Noriko Yamasaki[a], Makoto Yamauchi[z], Shigeo Yamauchi[az], Tahir Yaqoob[b], Yoichi Yatsu[ah], Daisuke Yonetoku[t], Atsumasa Yoshida[k], Takayuki Yuasa[q], Irina Zhuravleva[f], Abderahmen Zoghbi[h], and John ZuHone[b]

[a]Institute of Space and Astronautical Science (ISAS), Japan Aerospace Exploration Agency (JAXA), Kanagawa 252-5210, Japan
[b]NASA/Goddard Space Flight Center, MD 20771, USA
[c]Astronomy and Astrophysics Section, Dublin Institute for Advanced Studies, Dublin 2, Ireland
[d]SRON Netherlands Institute for Space Research, Utrecht, The Netherlands
[e]Department of Physics, Nagoya University, Aichi 338-8570, Japan
[f]Kavli Institute for Particle Astrophysics and Cosmology, Stanford University, CA 94305, USA
[g]Department of Earth and Space Science, Osaka University, Osaka 560-0043, Japan
[h]Department of Astronomy, University of Maryland, MD 20742, USA
[i]Université de Genève, Genève 4, Switzerland
[j]Department of Physics, Ehime University, Ehime 790-8577, Japan
[k]Department of Physics and Mathematics, Aoyama Gakuin University, Kanagawa 229-8558, Japan
[l]Kavli Institute for Astrophysics and Space Research, Massachusetts Institute of Technology, MA 02139, USA
[m]Lawrence Livermore National Laboratory, CA 94550, USA
[n]Institute of Astronomy, Cambridge University, CB3 0HA, UK
[o]Yale Center for Astronomy and Astrophysics, Yale University, CT 06520-8121, USA
[p]Department of Physics, University of Durham, DH1 3LE, UK
[q]RIKEN, Saitama 351-0198, Japan
[r]Department of Physics, Tokyo Metropolitan University, Tokyo 192-0397, Japan
[s]Harvard-Smithsonian Center for Astrophysics, MA 02138, USA

[t]Faculty of Mathematics and Physics, Kanazawa University, Ishikawa 920-1192, Japan
[u]Department of Physical Science, Hiroshima University, Hiroshima 739-8526, Japan
[v]Physics Department, University of Miami, FL 33124, USA
[w]Department of Astronomy and Physics, Saint Mary's University, Nova Scotia B3H 3C3, Canada
[x]European Space Agency (ESA), European Space Astronomy Centre (ESAC), Madrid, Spain
[y]Department of Physics and Astronomy, Aichi University of Education, Aichi 448-8543, Japan
[z]Department of Applied Physics, University of Miyazaki, Miyazaki 889-2192, Japan
[aa]Department of Physics, University of Tokyo, Tokyo 113-0033, Japan
[ab]Department of Physics, Rikkyo University, Tokyo 171-8501, Japan
[ac]Department of Physics and Astronomy, Rutgers University, NJ 08854-8019, USA
[ad]Department of Physics and Astronomy, Johns Hopkins University, MD 21218, USA
[ae]Faculty of Human Development, Kobe University, Hyogo 657-8501, Japan
[af]Kyushu University, Fukuoka 819-0395, Japan
[ag]Research Institute for Science and Engineering, Waseda University, Tokyo 169-8555, Japan
[ah]Department of Physics, Tokyo Institute of Technology, Tokyo 152-8551, Japan
[ai]Tsukuba Space Center (TKSC), Japan Aerospace Exploration Agency (JAXA), Ibaraki 305-8505, Japan
[aj]Department of Physics, Toho University, Chiba 274-8510, Japan
[ak]Department of Physics, Tokyo University of Science, Chiba 278-8510, Japan
[al]Department of Physics, Kyoto University, Kyoto 606-8502, Japan
[am]Department of Electronic Information Systems, Shibaura Institute of Technology, Saitama 337-8570, Japan
[an]IRFU/Service d'Astrophysique, CEA Saclay, 91191 Gif-sur-Yvette Cedex, France
[ao]Space Telescope Science Institute, MD 21218, USA
[ap]European Space Agency (ESA), European Space Research and Technology Centre (ESTEC), 2200 AG Noordwijk, The Netherlands
[aq]Department of Physics, Tokyo University of Science, Tokyo 162-8601, Japan
[ar]Department of Physics, University of Wisconsin, WI 53706, USA
[as]University of Waterloo, Ontario N2L 3G1, Canada
[at]Department of Astronomy, University of Michigan, MI 48109, USA
[au]Department of Astronomy, Kyoto University, Kyoto 606-8502, Japan
[av]Department of Information Science, Faculty of Liberal Arts, Tohoku Gakuin University, Miyagi 981-3193, Japan
[aw]Department of Physics, Faculty of Science, Yamagata University, Yamagata 990-8560, Japan
[ax]Laboratory of Nuclear Studies, Osaka University, Osaka 560-0043, Japan
[ay]NASA/Marshall Space Flight Center, AL 35812, USA
[az]Department of Physics, Faculty of Science, Nara Women's University, Nara 630-8506, Japan
[ba]Department of Astronomy, Columbia University, NY 10027, USA
[bb]Department of Physics and Astronomy, University of Manitoba, MB R3T 2N2, Canada
[bc]Department of Physics, Saitama University, Saitama 338-8570, Japan
[bd]Department of Physics, Chuo University, Tokyo 112-8551, Japan
[be]Science Education, Faculty of Education, Shizuoka University, Shizuoka 422-8529, Japan
[bf]Faculty of Social and Information Sciences, Nihon Fukushi University, Aichi 475-0012, Japan

Contents

1 Using *ASTRO-H* to Type Supernovae and Unveil their Progenitors **5**
- 1.1 Background and Previous Studies . . . 5
- 1.2 Prospects & Strategy . . . 6
  - 1.2.1 Typing Ia supernovae from abundance measurements of their remnants: addressing the prompt vs. delayed mechanisms . . . 6
  - 1.2.2 Mn-to-Cr mass ratios, odd-Z and radioactive species . . . 7
  - 1.2.3 Core-collapse remnants: Is the observed diversity of their neutron stars linked to their supernova progenitors? . . . 9
- 1.3 Targets & Feasibility . . . 10
  - 1.3.1 Tycho's SNR: A unique laboratory for high-resolution spectroscopy . . . 10
  - 1.3.2 SN 1006: odd-Z trace elements . . . 13
  - 1.3.3 Cas A: the famous oxygen-rich remnant with a central compact object . . . 13
  - 1.3.4 SN1987A: the youngest known supernova remnant . . . 17
  - 1.3.5 Radioactive species in the youngest Galactic remnant: SNR G1.9+0.1 . . . 18
  - 1.3.6 Kes 73: a core-collapse remnant associated with an anomalous X-ray pulsar (magnetar) 19
  - 1.3.7 Other *ASTRO-H* targets . . . 21
- 1.4 Beyond Feasibility . . . 22

2 Ejecta Distribution in Space and Velocity **22**
- 2.1 Background and Previous Studies . . . 22
- 2.2 Prospects & Strategy . . . 24
  - 2.2.1 Structural diversity in Ia remnants . . . 25
  - 2.2.2 SN 1006: An exceptional target . . . 26
- 2.3 Targets & Feasibility . . . 27
  - 2.3.1 SN 1006: determining the expansion velocity in multiple elemental species . . . 27
  - 2.3.2 SNR 0519–69.0: bulk motion expansion . . . 28
  - 2.3.3 Other *ASTRO-H* targets . . . 28
- 2.4 Beyond Feasibility . . . 29

3 How Does the Thermal Plasma State of a Supernova Remnant Link with the Efficiency of its Particle Acceleration? **29**
- 3.1 Background and Previous Studies . . . 29
- 3.2 Prospects & Strategy . . . 30
- 3.3 Targets & Feasibility . . . 31
  - 3.3.1 Cas A: non-thermal X-ray emission . . . 31
  - 3.3.2 RX J1713.1–3946: the search for thermal line emission . . . 31
  - 3.3.3 Other *ASTRO-H* targets . . . 33
- 3.4 Beyond Feasibility . . . 33

4 Summary **34**

1 Using *ASTRO-H* to Type Supernovae and Unveil their Progenitors

1.1 Background and Previous Studies

Unlike unresolved X-ray sources, supernova remnants (SNRs), because of their significant extent, have not benefited from the high-resolution spectroscopic capabilities provided by the gratings on *XMM-Newton* and *Chandra*. Indeed virtually all studies of SNRs have been carried out with CCD-type spectral resolution (i.e., $E/\Delta E \sim 10$). This is sufficient to resolve He-like and H-like lines of the major elemental species (O, Ne, Si), but it has not allowed us to perform true spectral analysis based on individual resolved emission lines. This is especially frustrating for SNR aficionados, since SNR spectra are arguably among the most complex in astrophysics with dependencies on elemental composition, electron temperature, ion temperature, ionization and recombination timescales, turbulent and bulk velocity flows, and the significant presence of non-thermal particle distributions. Thus high spectral resolution observations with *ASTRO-H*'s Soft X-ray Spectrometer (SXS) will provide a huge "game-changing" leap forward for X-ray studies of SNRs.

As the principal production and dispersal sites of stellar and explosive nucleosynthesis, SNRs hold important keys to our understanding of the numerous theoretical processes involved in the production of the chemical elements (see Wallerstein et al. 1997 for an update of Burbidge et al. 1957). In general, however, this theory has been tested largely against ensemble-averaged measurements, such as the relative abundance distribution of the elements in various environments (e.g., solar), the atmospheres of stars, and so on. Nucleosynthesis is a rich, complex field that involves many disparate processes operating in different environments and at different phases of stellar evolution. Observational tests of specific model components, especially of the most energetic processes, are woefully lacking. In particular, the processes that produce Fe and Fe-group elements and eject them into the interstellar medium during the explosions of both core-collapse and thermonuclear supernovae (SNe) are among the most poorly tested parts of the entire nucleosynthesis picture. X-ray studies of young SNRs (see Vink 2012 and references therein for a review) can provide critical tests of the nucleosynthesis picture especially as regards the production of Fe and Fe-group elements in specific individual examples of core-collapse and thermonuclear SNe. In addition since the production of Fe and Fe-group elements is at the heart of these explosions, they offer critical insights into the explosion processes in SNe.

Core-collapse (CC) SNe make up roughly three-quarters of all observed SNe. They come from stars more massive than $\sim 8 M_{\odot}$ and from a nucleosynthetic point of view are the dominant producers of O, Ne, and Mg, although they do produce a broad spectrum of elemental species including the Fe-group. They leave compact remnants in the form of neutron stars (or black holes for the most massive progenitors), while their gaseous remnants tend to be highly structured with dense optically-emitting knots and typically more diffuse X-ray features. It is known that the precipitating event for a CC SNe is the collapse of a stellar core, but the process whereby the core rebounds and ejects the rest of the star is still poorly understood with at least two competing ideas currently in vogue: neutrino-driven convection (e.g., Herant et al. 1994; Burrows, Hayes, & Fryxell 1995; Kifonidis et al. 2000), including in its latest development the instability of the stalled shock (e.g., Blondin & Mezzacappa 2006; Foglizzo, Scheck, & Janka 2006; Burrows et al. 2007; Scheck et al. 2008); and jet-induction (e.g., Khokhlov et al. 1999). It is also the case that at present nucleosynthesis predictions still rely on spherically symmetric models with an assumed neutron star/black hole "mass cut" (e.g., Woosley & Heger 2007).

The other main class of SNe are the thermonuclear or Type Ia SNe (SN Ia). These make up roughly one-quarter of all SNe and are widely believed to result from the total incineration of a carbon-oxygen white dwarf that grows close to the Chandrasekhar mass. How the star increases its mass is unknown; single degenerate scenarios where the white dwarf accretes matter from a normal-star companion in a binary and double degenerate scenarios where two white dwarfs coalesce are the two favored possibilities. During the explosion about half of the star's mass is converted to ^{56}Ni which decays to stable ^{56}Fe. Even with hundreds of well-observed type Ia SNe and the intense focus of the theoretical community over the past 15 years, the SN Ia explosion process, i.e., how nuclear ignition occurs and the subsequent burning proceeds, remains an unsolved problem (e.g., Röpke, & Bruckschen 2008; Jordan et al. 2008). Models that most successfully reproduce optical spectra of SNe Ia essentially parameterize the speed of the burning front through the star (e.g., Iwamoto et al. 1999). These models also usually include a parameterized transition from a subsonic burning front (deflagration) to a

supersonic burning front (detonation).

Observational results on the X-ray properties of young SNRs obtained to date, as important and relevant as they are, suffer, fundamentally, from a lack of precision. CCD-type spectral resolution is unable to provide accurate measurements of even the most basic thermodynamic quantities that characterize the plasma, i.e., electron temperature and the charge states of the relevant ions. This introduces large errors in relative abundance measurements. Studies of dynamics are limited to only the most extreme speeds (1000's of km s^{-1}). Significant advances require improved spectral resolution in order to resolve individual lines and derive plasma diagnostics from line ratios.

Although the X-ray emission from SN ejecta provides powerful diagnostics of the progenitor's nature, we should keep in mind that what we see is only the part of the ejecta that has been shock-heated to X-ray emitting temperatures. Our discussions, therefore, must be influenced by the dynamical state of the particular SNR under study. In most young Type Ia SNRs (such as Tycho, SN 1006, and 0509−67.5), the reverse shock is still propagating through the Fe-rich central region (where C-O has been burnt to nuclear statistical equilibrium), while the other elements (Si, S, Ar, and Ca) at the outer incomplete Si-burning layer have already been fully heated (e.g., Hwang & Gotthelf 1997; Warren & Hughes 2004). Therefore, the observed abundance ratios between Fe and the intermediate mass species cannot be used to, for example, infer the transition density from deflagration to detonation to which it is most sensitive. Similar issues of "hidden" or unshocked ejecta exist for core-collapse SNRs, and in these cases the assumption of stratified ejecta will be even more untenable. Nevertheless, *ASTRO-H* SXS spectra of young SNRs will allow us to determine the temperature and ionization age of *each* species visible and thereby constrain the spatial variation of thermodynamic conditions throughout the remnant. This will offer more "grist" to constrain hydrodynamical simulations, such as those of Badenes et al. (2003, 2006).

1.2 Prospects & Strategy

Here we present three important scientific research topics that *ASTRO-H* can address regarding young supernova remnants. Most of these require the high spectral resolution of the SXS.

1.2.1 Typing Ia supernovae from abundance measurements of their remnants: addressing the prompt vs. delayed mechanisms

Original work on typing SNe from their remnants (Hughes et al., 1995) identified three SNRs in the Large Magellanic Cloud (LMC) as originating from type Ia explosions using the gross difference in the expected X-ray spectra of CC (more O-rich) vs. Ia (more Fe-rich) SNe. One of the candidates (SNR 0509−67.5) was subsequently confirmed as a *spectroscopic* Ia by measurement of the light echoes from the original SN (Rest et al., 2008a). Another of the candidate SN Ia remnants (N103B) is unusual in that it lies near a young, rich star cluster in the LMC and appears to be interacting with dense circumstellar gas. There is also some disagreement in interpretation between the *Chandra* ACIS spectro-imaging data (Lewis et al., 2003) and the *XMM-Newton* integrated RGS spectrum (van der Heyden et al., 2002). Both studies find significant emission from oxygen, silicon, and iron, as well as other species. van der Heyden et al. (2002) chose to interpret their global spectrum as coming entirely from SN ejecta and concluded that the presence of large amounts of oxygen argued for a core-collapse origin. On the other hand Lewis et al. (2003) found strong evidence for a shell-like remnant structure in the emission from Si, S, and Fe, while the O emission was distributed in an entirely different manner and was more closely correlated with the continuum. These authors argued that the oxygen emission was therefore from a different component, namely the swept-up interstellar medium, and that the SN Ia hypothesis was still viable and indeed preferred. Indeed the properties of N103B bear some resemblance to Kepler's SNR, another putative SN Ia remnant with interstellar interaction (Reynolds et al., 2007).

The Tycho SNR also shows light echoes (Rest et al., 2008b). Optical spectra of these have revealed the originating SN to belong to the majority class of normal type Ia SN (Krause et al., 2008), a result that confirms earlier predictions by Badenes et al. (2006) based on their interpretation of the X-ray spectrum of Tycho. For the remnant mentioned above, 0509−67.5, on the other hand, light echo spectra showed that it belongs to the

bright, highly energetic subclass of Type Ia explosions, similar to SN 1991T. This subclass is widely suspected of producing a larger mass of ^{56}Ni during the explosion, which, again, is consistent with the X-ray properties of the remnant (Badenes et al., 2008a).

Studies of large samples of Type Ia SNe have revealed the need for at least two evolutionary paths to these explosions: a prompt component (whose rate is proportional to the star formation rate) and a delayed one (proportional to the total stellar mass) (e.g., Scannapieco & Bildsten 2005). It has been suggested (e.g., Aubourg et al. 2008) that the prompt type could have progenitors that are relatively young massive stars with high metallicity. Therefore, the single degenerate scenario is often linked to the prompt population, while the double degenerate to the other. Moreover, recent systematic observations suggest that star-forming (and/or high-z) galaxies tend to host bright Type Ia SNe (e.g., Howell et al. 2009; Sullivan et al. 2010), implying that single-degenerate progenitors can more easily induce bright SNe. X-ray observations of SNRs offer a powerful test of this hypothesis. Some Type Ia SNRs (e.g., Kepler, RCW 86, N103B) are suspected of being associated with star-forming regions (e.g., Rosado et al. 1996; Chu & Kennicutt 1988). Do they belong to this recently recognized subclass of Ia SNe (i.e., prompt)? There are already some pieces of evidence that Kepler and RCW 86 have single degenerate origins (Williams et al., 2011, 2012). These important questions and details are best addressed with *ASTRO-H*.

For completeness we note that *Chandra* has revealed other, older Magellanic Cloud SNRs to be type Ia based on the composition of the ejecta contained within their interiors: DEM L71 (Hughes et al., 2003); DEM L238 and DEM L249 (Borkowski et al., 2006); and 0104−72.3 (Lee et al., 2011). Others have been shown to be of core-collapse origin: e.g., 0103−72.6 (Park et al., 2003). Some of these objects may be interesting targets in conjunction with studies of Magellanic Cloud and Galactic middle-aged (∼10 kyr-old) remnants, where evidence for metal-rich SN ejecta is being sought or found (e.g. 0454–67.2 in the LMC, Seward et al. 2006; see also Section 1.3.7).

With *ASTRO-H* SXS, we will make precise abundance measurements of Type Ia SNRs that include "normal" type Ia remnants, such as Tycho SNR, SN 1006, and SNR 0519−69.0, and possible "prompt" ones like Kepler and N103B. With sensitive line strength measurements, combined with accurate ionization and temperature diagnostics, we will make accurate abundance determinations. Comparison to theoretical models of nucleosynthetic yields (e.g., Iwamoto et al. 1999; Maeda et al. 2010b) will provide insight into the possible explosion models for SNe Ia and the differences between the prompt and delayed evolutionary channels.

1.2.2 Mn-to-Cr mass ratios, odd-Z and radioactive species

The excellent resolving power of *ASTRO-H*'s SXS will allow a detection and study the chemical elements beyond the most abundant even-Z species O, Ne, Mg, Si, S, Ar, Ca and Fe with which X-ray astronomers have been working almost exclusively, to date. Recent exceptions to this general rule are the detection of the trace abundance species Cr ($Z = 24$) and Mn ($Z = 25$) in several SNRs using CCD spectra. Cr and Mn are the species with the highest abundances (DEX abundances of 5.67 and 5.39, respectively, Anders & Grevesse 1989) between Ca and Fe.

W49B was the first remnant in which Cr and Mn emission lines were detected (Hwang et al., 2000b); see the Old SNRs+PWNe White Paper (WP #8) for a discussion of this SNR. Currently, thanks to *Suzaku* observations (see Table 2 in Yang et al. 2013), there are six SNRs with Mn line detections (Kepler, W49B, N103B, 3C 397, Tycho, and G344.7−0.1) and an additional two SNRs for which only Cr has been detected (Cas A and SNR 0519−69.0). In the following Table we list these 8 SNRs in order of their Cr line strength. The three columns show the total SXS count rate in each of the three lines (using `sxt-s_120210_ts02um_of_intallpxl.arf` and assuming all of the photons arrive at the mean energy as shown).

SNR name	Cr rate (5.6 keV)	Mn rate (6.1 keV)	Fe rate (6.6 keV)
W49B	1.5×10^{-2}	4.8×10^{-3}	4.0×10^{-1}
Cas A	1.1×10^{-2}	...	7.8×10^{-1}
Tycho	8.0×10^{-3}	7.7×10^{-4}	2.2×10^{-1}
3C 397	4.8×10^{-3}	2.8×10^{-3}	5.9×10^{-2}
Kepler	1.6×10^{-3}	8.7×10^{-4}	1.3×10^{-1}
G344.7−0.1	1.2×10^{-3}	3.5×10^{-3}	8.8×10^{-3}
N103B	5.2×10^{-4}	3.2×10^{-4}	1.0×10^{-2}
0519−69.0	2.6×10^{-4}	...	4.1×10^{-3}

Metallicity is one possible difference in the properties of the progenitor between the prompt and delayed channels for Type Ia SN explosions. A recent powerful advance in this area came from the recognition that the Mn-to-Cr mass ratio in Type Ia explosion models tightly correlates with the initial metallicity of the original white dwarf's progenitor (Badenes et al., 2008b). The basic idea is that the mass ratio of Mn to Cr produced though nuclear burning during the explosion depends sensitively on the electron-to-nucleon fraction (Y_e) in the white dwarf. Timmes, Brown, & Truran (2003) have already shown that Y_e is linearly proportional to the metallicity of the white dwarf progenitor. Applying this technique to the *Suzaku* spectrum of the Tycho SNR where Mn and Cr were both detected (Tamagawa et al., 2009), Badenes et al. (2008b) were able to show that the metallicity of Tycho's progenitor star was supersolar. Although the errors were large, values of metallicities much below solar can be rejected. Since then deeper *Suzaku* observations of Tycho, Kepler, and several other Ia SNRs have been taken and refined estimates of the progenitor metallicities are being obtained (see, for Kepler, Park et al. 2013).

It is also claimed that the delayed (and hence dim and probably double-degenerate) SNe Ia yield lower abundance ratios of Cr/Fe, Mn/Fe, and Ni/Fe than the prompt (brighter, single-degenerate) SNe Ia (Tsujimoto & Shigeyama 2012). Therefore, not only the Mn/Cr abundance ratio but also the (Cr+Mn+Ni)/Fe ratio should be compared among different types of Type Ia SNRs.

If the Mn and Cr lines are unbroadened, then the *ASTRO-H* SXS will have greater sensitivity (than CCDs) to the line detection and will have better ability to measure the charge states of these species for comparison to the charge state of Fe. In fact a joint study of the SXS and Soft X-ray Imager (SXI) spectra of these objects may be most effective in clarifying the ionization conditions and thereby derive accurate relative masses for these species.

The detectability of Cr and Mn K-shell lines in CCD spectra is possible, not only because the cosmic abundance of these species is sufficiently high, but also because their K-shell line energies (~5.6 keV and ~6.1 keV) fall in a generally line-free region of the X-ray band. Detecting and studying odd-Z species with lower atomic number is made much more difficult by confusion with stronger lines at nearby photon energies from the more abundant even-Z species. The high spectral resolution of the SXS will help overcome these effects of confusion and make the first robust detections of these species.

In order of decreasing abundance (assuming solar values from Anders & Grevesse 1989), the odd-Z species we intend to study are Al (abundance in DEX = 6.47; He-like K-shell energy = 1.6 keV) and Na (6.33, 1.1 keV), then P (5.45, 2.1 keV), all of which are more abundant than Mn (5.39). Just slightly below this threshold are Cl (5.27, 2.8 keV) and K (5.12, 3.5 keV). Most of these species K-shell lines (with the possible exception of Na) are far from the Fe-L blend and hence it will be possible to establish unique line identifications for them. Given that yields of all the neutron-rich elements depend on the progenitor's metallicity, these odd-Z elements could also be a useful metallicity probe. Notably, Al emission can be observed around 1.6 keV, where the effective area of the SXS is much larger than that in the Mn-Kα band. Moreover, lighter elements should have lower ion temperatures, and hence expected thermal broadening will be smaller (although Doppler broadening from turbulence and bulk motion will still pertain). A previous *Suzaku* observation of a possible Type Ia SNR, G344.7−0.1, already detected strong Al emission from this remnant (Yamaguchi et al. 2012, although this emission may originate from swept-up ISM). The SXS will enable us to detect this line from most of the other Ia SNRs.

If a SNR is young enough, emission from radioactive species can become detectable. The prime candidate species for this is ^{44}Ti, which decays through electron capture to ^{44}Sc. Electron capture leaves a K-shell vacancy in the Sc atom that relaxes through the emission of a fluorescence line at 4.1 keV (which is in the SXS band). This is fully independent of the reverse-shock heating and provides an estimate of the amount of ^{44}Ti synthesized by the SN. The decay of ^{44}Ti also produces nuclear γ-rays at energies of 67.9, 78.4 and 1157 keV; the former two lines can, in principle, be detected by the HXI. Finally ^{44}Ti is synthesized at extremely high temperatures in the deepest layers of the exploding star and, in the case of core-collapse SNe, near the mass cut. Recent simulations of off-center delayed-detonation Type Ia explosions showed a synthesized ^{44}Ti mass of $\sim 2 \times 10^{-5}\ M_\odot$ (Maeda et al., 2010b). On the other hand, core-collapse SN models predict a larger mass $> 6 \times 10^{-5}\ M_\odot$ (Timmes et al., 1996), or even more if the explosion is asymmetric (Nagataki et al., 1998).

1.2.3 Core-collapse remnants: Is the observed diversity of their neutron stars linked to their supernova progenitors?

Here we discuss how to use *ASTRO-H* to infer the progenitor masses of SNRs associated with neutron stars of several different types.

Core-collapse SNRs provide unique laboratories to study, not only the heavy elements created in the Universe and the physics of shocks and particle acceleration, but also the origin of the most exotic, compact, and highly-magnetized stars in the Universe: neutron stars and their associated nebulae. When a star with a ZAMS mass in the range $\sim 8 - 20\ M_\odot$ ends its life, in addition to expelling several solar masses of gaseous ejecta, it leaves behind a neutron star (Woosley et al., 2002). The most famous example of a CC SNR is the Crab nebula believed to be associated with SN 1054AD.

While Ia SNRs are believed to expand in relatively uniform media, core-collapse explosions expand in media strongly modified by mass loss from the SN progenitor, naturally affecting their dynamics, morphology and spectral signatures (e.g. Dwarkadas 2005, Lopez et al. 2011). The presence of a compact object in the SNR interior, surrounded by a synchrotron nebula for the rotation-powered neutron stars, further complicates the analysis of these objects, but also offers another tool for probing their SN progenitors and explosion properties (e.g. Chevalier 2005).

The past decade has witnessed the discovery of a growing diversity of neutron stars associated with SNRs (e.g. Mereghetti 2013). These include the "classical" rotation-powered pulsars typically discovered at radio wavelengths and with dipole surface magnetic fields $B{\sim}10^{12}$ G (like the Crab)[1], the X-ray and gamma-ray discovered 'magnetars', commonly believed to be neutron stars with super-strong $B{\sim}10^{14}$–10^{15} G and with two flavors (the anomalous X-ray pulsars [AXPs] and the soft gamma-ray repeaters), high-B pulsars (HBPs) with magnetic fields intermediate between the Crab-like pulsars and magnetars and close to the quantum electrodynamic value of $4.3{\times}10^{13}$ G (like PSR J1846–0258 in SNR Kes 75), and the Central Compact Objects (CCOs) discovered in X-rays near the centers of their hosting SNRs (like the CCO discovered with *Chandra* in the O-rich and young SNR Cas A) and dubbed as 'anti-magnetars' with $B{\sim}10^{10}$–10^{11} G. Understanding the origin for this diversity remains one of the hottest topics in the field today. While studying any connection between these apparently different classes is being conducted with dedicated studies of the compact objects themselves[2], another promising approach to this puzzle is through studying their hosting SNRs. SNRs should provide clues on their environment, energetics and the supernova explosions that created them. In particular, it is not clear whether the diversity of neutron stars is related to a diversity in supernova progenitors of core-collapse supernovae.

Of particular interest, there has been recently growing evidence for the highly magnetized neutron stars (i.e. HBPs and magnetars) to originate from *very* massive stars (of mass exceeding $\sim$20 $M_\odot$). Although this remains controversial, X-ray and multi-wavelength studies seem to be pointing to this conclusion (see, e.g., Gaensler et al. 2005; Kumar et al. 2012; Safi-Harb & Kumar 2013). X-ray spectroscopy of SNRs provides a powerful

[1] the question on the absence of SNR shells in Crab-like nebulae is by itself a puzzling question that is being addressed in the "Old SNRs and PWNe" White Paper #8

[2] see the "High-Mass X-ray Binaries and Magnetars" White Paper #4 for a detailed discussion on this topic

tool to infer the mass of the progenitor star. This is achieved through modelling the X-ray spectra of ejecta-dominated SNRs; and subsequently comparing the inferred abundances of the metals detected in the 0.3–10 keV band (O through Fe) to nucleosynthesis models (e.g. Woosley & Weaver 1995; Nomoto et al. 2006).

Below we show how to take advantage of the Soft X-ray Spectrometer (SXS)'s unprecedented spectral resolution and sensitivity to the emission lines expected from young SNRs to type the progenitors and determine or pin down their masses in a number of promising targets. The proposed science will further illustrate the leap that will be achieved in high-resolution X-ray spectroscopy of *extended sources* such as SNRs, a task that is challenging with gratings on-board *XMM-Newton* and *Chandra*.

1.3 Targets & Feasibility

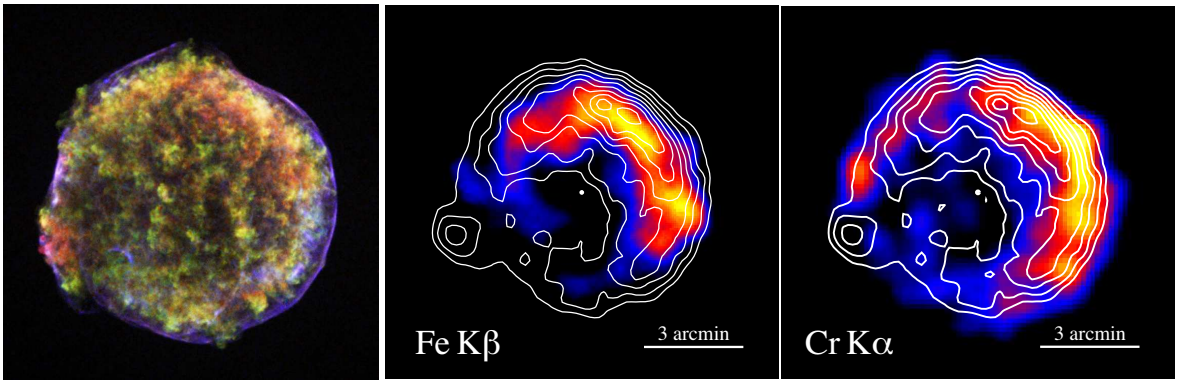

Figure 1: X-ray images of Tycho's SNR from *Chandra (left panel)*, the *Suzaku* XIS in the Fe-Kβ band (7.0–7.2 keV) *(middle panel)* and Cr-Kα band (5.4–5.6 keV) *(right panel)*. The *Chandra* image shows the Fe L band in red, Si K in green and 0.4-6.0 keV continuum band in blue. The non-thermal continuum is subtracted from the *Suzaku* images. The Fe-Kα image (6.43–6.53 keV) is over-plotted in contours. The Fe-Kβ emission peaks at a smaller radius than the Fe-Kα emission in the bright NW rim, while the Cr-Kα emission peaks at a larger radius (Yamaguchi et al. 2014). The profile of the Fe-Kβ emission reflects the spatial distribution of the low-ionized Fe ions (see the NSF White Paper for details), so is also important as an indicator of the reverse shock position.

1.3.1 Tycho's SNR: A unique laboratory for high-resolution spectroscopy

Tycho is the brightest and most prototypical (in fact "normal") Type Ia SNR in the Milky Way. The thermal spectrum is fully dominated by the ejecta with little evidence of emission from shocked ISM (Cassam-Chenaï et al., 2007). Tycho also shows evidence of local inhomogeneity in the ejecta (e.g., Vancura et al. 1995), specifically in the form of two compact knots, one Fe-rich, the other Si-rich, lying at the edge of the SNR rim in the SE quadrant (see Figure 1–left panel). The narrowband images of Tycho's SNR obtained by *ASCA* show that the Fe-Kα emission is located interior to the emission lines of intermediate-mass elements (Hwang & Gotthelf, 1997). This was confirmed by higher-resolution observations by *Chandra* (Warren et al., 2005) and *XMM-Newton* (Decourchelle et al., 2001). With *Suzaku*, Tamagawa et al. (2009) detected emission from Cr and Mn, which were later shown to be important elemental species with which to probe the progenitor's metallicity (Badenes et al., 2008b). The *Suzaku* data also allowed measurement of the ejecta expansion velocity from line broadening due to superposition of red- and blue-shifted components. Hayato et al. (2010) found the expansion velocities of Si, S, and Ar ejecta ($4700 \pm 100\,\mathrm{km\,s^{-1}}$) to be distinctly higher than that obtained from the Fe-Kα emission ($4000 \pm 300\,\mathrm{km\,s^{-1}}$), which is consistent with segregation of the Fe in the inner ejecta.

In 2008 a deeper *Suzaku* observation was performed with the original purpose of accurately measuring the Cr and Mn abundances in the ejecta. This new observation also enabled the first-ever detection of Fe-Kβ emission, which has turned out to be useful as a diagnostic of the ionization population. Yamaguchi et al. (2013) found that the observed intensity ratio of Kβ/Kα is larger than that expected from the dominant charge state of the Fe ejecta (Fe^{16+}) determined from the Kα centroid energy. This indicates that a significant fraction of the Fe

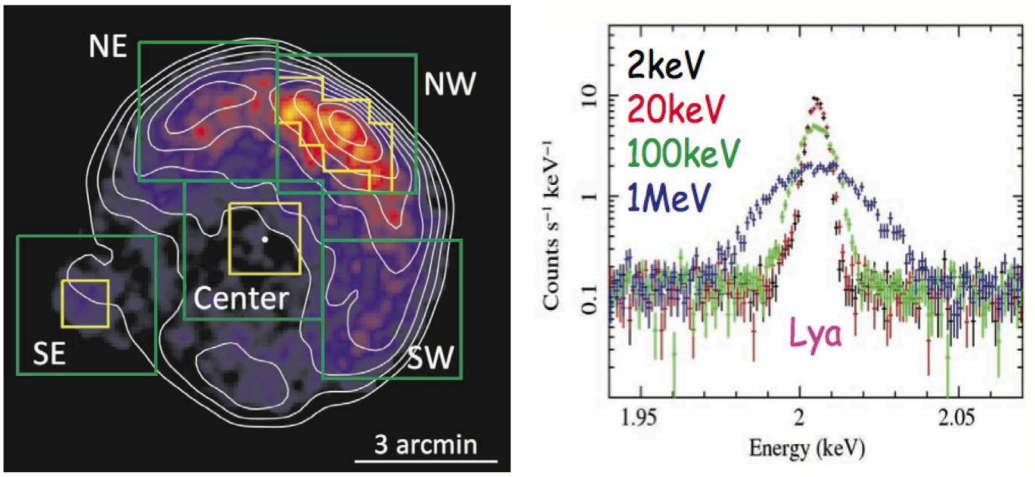

Figure 2: *(Left) Suzaku* XIS image of Tycho's SNR in Fe-Kα (6.43–6.53 keV) (in color) with the Si Kα image (1.75–2.05 keV) overplotted as contours. Five possible *ASTRO-H* SXS pointings are shown with the green boxes. *(Right)* 100-ks SXS simulation of the Si Ly-α line showing the effect of changing the line broadening depending on the Si ion temperature.

ejecta is in an even lower charge state. It was also revealed that Cr-α emission clearly peaks at a larger radius compared to the Fe emission (Figure 1 right). This is against the recent claim by Yang et al. (2013) that Cr and Fe are always spatially correlated. With a high-resolution observation by SXS, we can accurately determine the ionization age of each element: if Cr indeed is distributed in the outer region, it should be more highly ionized than Fe. The SXS observation will also allow us to measure accurate abundances of these elements, which are important to constrain the progenitor's nature.

Tycho is approximately 8′ in diameter with a number of interesting regions (see Figure 2–left panel) that are worthy of study: (1) the bright NW rim where the X-ray intensity is highest and the shock front is most circularly shaped, (2) the SE region where there are two knots of ejecta (one Si-rich, one Fe-rich) that seem to have expanded further than the rest of the shell (3) the center, (4) the SW region where the synchrotron emission is most intense and extends to the highest energies, and (5) the NE region where there is some evidence for interaction with molecular clouds (Xu, Wang, & Miller 2011).

With a 100-ks exposure at the NW rim, we can cleanly measure the Si ion temperature with an estimated error of 10% (see Figure 2–right panel). Still the NW rim merits a deeper observation (400 ks) with the SXS in order to determine the extent of collisionless heating at the reverse shock, which is propagating into the Fe-rich ejecta. We will measure the charge state of Fe from both the Kα and Kβ lines and measure the ion temperature from the line widths. We will be able to distinguish Fe temperatures varying from 10 keV up to 1 MeV and detect the low ionization population, although this will be quite challenging in the high temperature case (see Figure 3). Note that the long exposure time is driven by the need to measure the faint Fe-Kβ line complex which comes predominantly from the lower Fe ionization states.

For the SE region, where the ejecta knots are, we simulated a 100 ks exposure and showed that the Fe ion temperature can be determined to 10-15% accuracy for Fe ion temperatures in the range 200 keV to 3 MeV (see Figure 4). Since these knots are at the rim (moving perpendicular to our line-of-sight) and fairly isolated, bulk motion broadening should not be a significant concern. The origin of these ejecta knots is still mysterious and the aim of this pointing is to measure the ionic charge states and electron and ion temperatures for comparison with the more "normal" ejecta on the NW rim.

The center pointing is important to determine the physical expansion velocity for comparison to the known angular expansion rate. This will yield an accurate and precise measurement of the SNR's distance. This pointing will also allow for better determination of the reverse shock velocity, which will be important for interpreting the thermal line broadening we measure. The statistical uncertainty on the centroids of the strong Si and S lines will quickly reach the systematic error level in short exposures (10's of ks), but to adequately

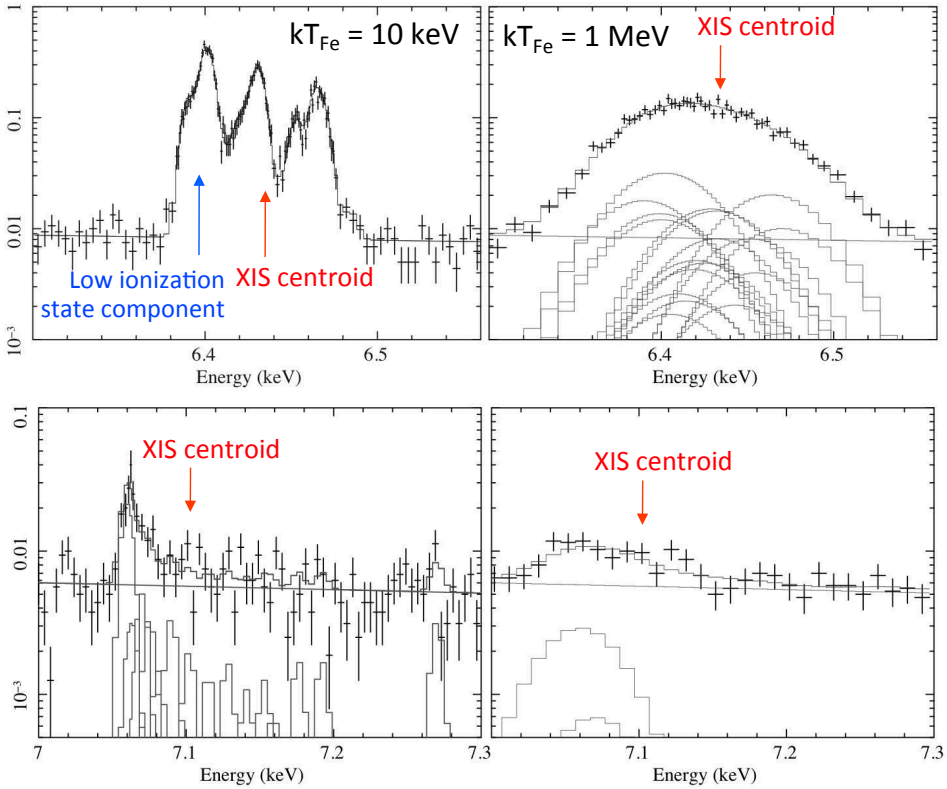

Figure 3: SXS simulation (400 ks) of the NW rim of Tycho for Fe-Kα *(top panels)* and Fe-Kβ *(bottom panels)* assuming two different ion temperatures: 10 keV *(left panels)* and 1 MeV *(right panels)*.

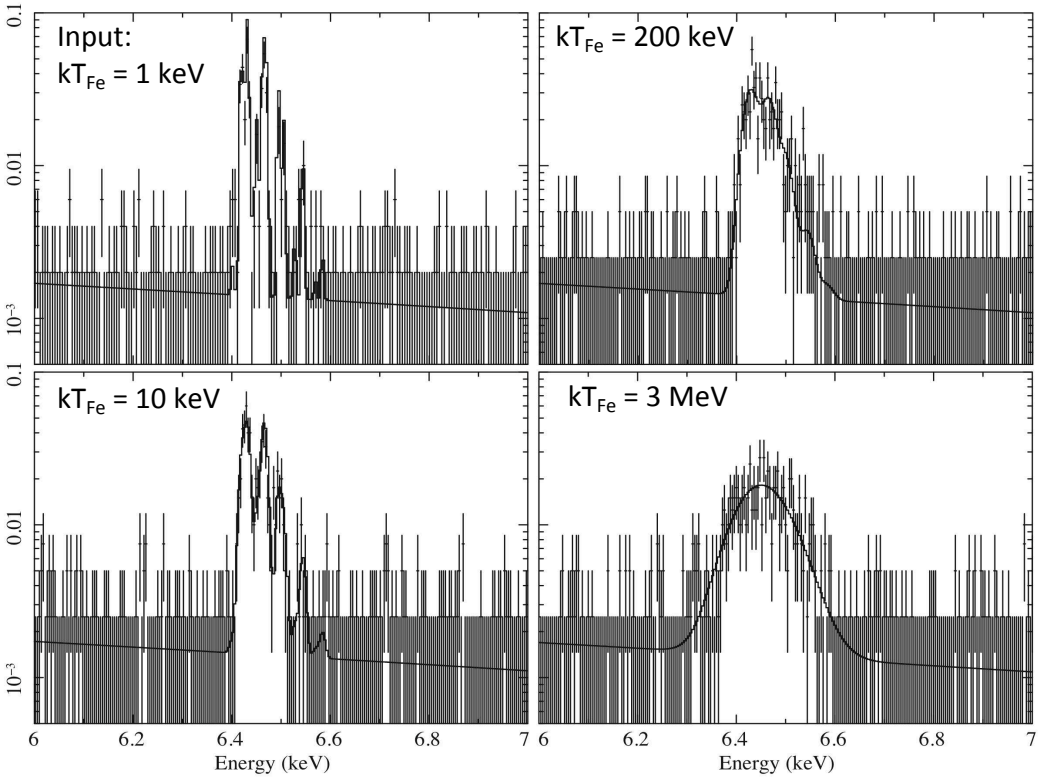

Figure 4: SXS simulations (each 100-ks) of the Fe-rich knot on the SE rim of Tycho assuming four different ion temperatures from 1 keV to 3 MeV as labeled. Only the energy band around the Fe-Kα is plotted.

sample the Fe line and other fainter features (i.e., trace odd-Z elements) will require exposures of the order of 100 ks.

The three regions mentioned above are of the highest scientific priority for advancing our understanding of the thermal emission of Tycho. Additionally, the SW region will be of interest also to White Paper #18, the Shock Acceleration task force team; the main goal will be to see if the thermal properties of the hot shocked plasma are different here compared to the rest of the remnant due to the more significant and efficient acceleration processes occurring in the SW. Finally, a complete mapping of Tycho, which can be achieved with some 9 SXS pointings, will further allow us to 1) do a precise determination of the ionization state and abundance measurements, search for odd-Z and low-abundance elements, map Cr and Mn across the SNR, and 2) map the hard (above 7 keV) X-ray emission with SXS and HXI. This, together with the measurement of the velocity structure through Doppler shifted lines from the central regions, will address all main topics covered in this White Paper.

1.3.2 SN 1006: odd-Z trace elements

We aim for several "pencil" beam SXS measurements of this remnant. Its large size (approx. 30′ in diameter) means that the modest angular resolution of *ASTRO-H* will not be a large negative factor. One pointing should be at or near the center to determine the expansion velocities of the approaching and receding hemispheres (this is presented in Section 2.3.1). A second pointing should be near the SE where *Suzaku* observations suggest a high Si abundance and the possible detection of Cr and Mn. The NW rim is an excellent candidate for studying the interaction of the forward shock with interstellar material to compare the thermal broadening of the O and Ne lines (likely interstellar) and Si and S (likely ejecta). An additional pointing near one of the bright synchrotron rims to study the efficiency of cosmic ray acceleration is alway worth pursuing.

SN 1006 also figures prominently in section 2 of this white paper. Here we restrict ourselves to presenting some simulations relevant to the detection of low abundance elemental species. Uchida et al. (2013) used the *Suzaku* XIS data to study SN 1006's spectral and spatial variations. One of their findings is highlighted in Figure 5 (left panel) which indicates the possible presence of Cr and Mn emission lines from the SE region of the remnant. As shown in the right panel of the same figure, a 200 ks exposure with the SXS would permit detection of these trace species assuming the best-fit model to the XIS data.

Along similar lines, an investigation into the possibility of detecting lower atomic number odd-Z species was made. This is shown in Figure 6. The left panel shows the *Suzaku* XIS data fitted to a two component model to account for the approaching and receding parts of the SNR. The parameters of the 2 vpshock models were the same except for the intensity scaling which needed to be different for the red- and blue-shifted components. Evidently there is an asymmetry in SN 1006 since the amount of X-ray emitting shocked material in the front and back halves is noticeably different. Al emission was included as three Gaussian lines (the forbidden, inter-combination, and resonance lines) for each velocity component. The intensities were determined using the APEC code at a temperature of 1 keV. Al was assumed to be enhanced by a factor of 3 above solar values. The right panel of Figure 6 shows that a significant detection of Al is possible in a 200 ks SXS exposure.

1.3.3 Cas A: the famous oxygen-rich remnant with a central compact object

The young (∼330 yr-old) supernova remnant Cassiopeia A is a bright core-collapse remnant whose X-ray emission clearly reveals large-scale spatial composition differences. *Chandra* observations show distinct regions of Si- and Fe-rich ejecta where Fe lies beyond Si at the eastern limb of the remnant (Hughes et al., 2000b). The Fe was formed in the innermost ejecta but was evidently overturned on large scales relative to the Si layer that was originally produced at higher locations in the exploding star. Doppler velocity measurements using *XMM-Newton* show that the Fe and Si emission in the northern part of the remnant are segregated in a same way as at the eastern rim (Willingale et al., 2002). Optical spectra of light echoes indicate that the Cas A SN was a Type IIb that originated from the collapse of the helium core of a red supergiant that had lost most of its hydrogen envelope before the explosion (Krause et al., 2008). A central compact object was revealed by the first *Chandra* image of Cas A (Tananbaum, 1999). Evidence from subsequent *Chandra* observations spanning

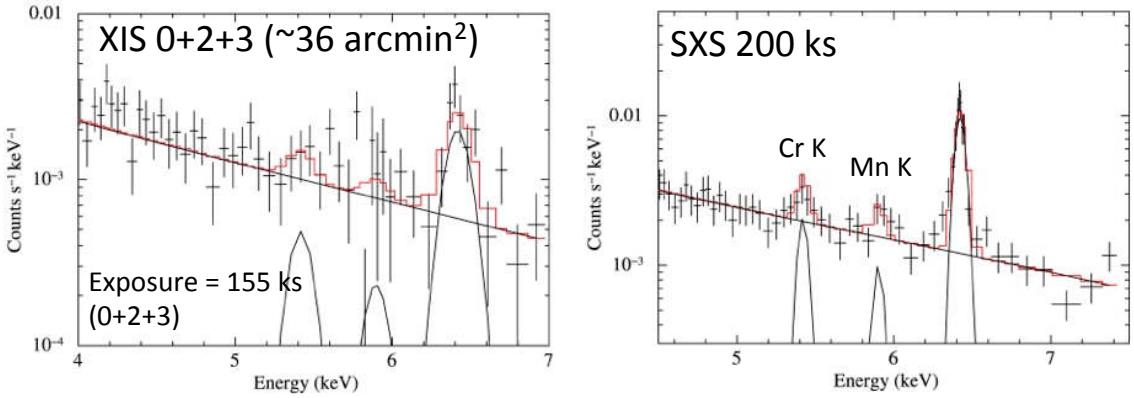

Figure 5: *(Left) Suzaku* XIS spectra extracted from a 3′ × 3′ region at the SE rim of SN 1006 showing the clear detection of the Fe-Kα line and evidence for Cr and Mn emission. *(Right)* SXS simulation of the best fit XIS model assuming a 200 ks exposure with *ASTRO-H*. All the lines were assumed to be broadened by 34 eV.

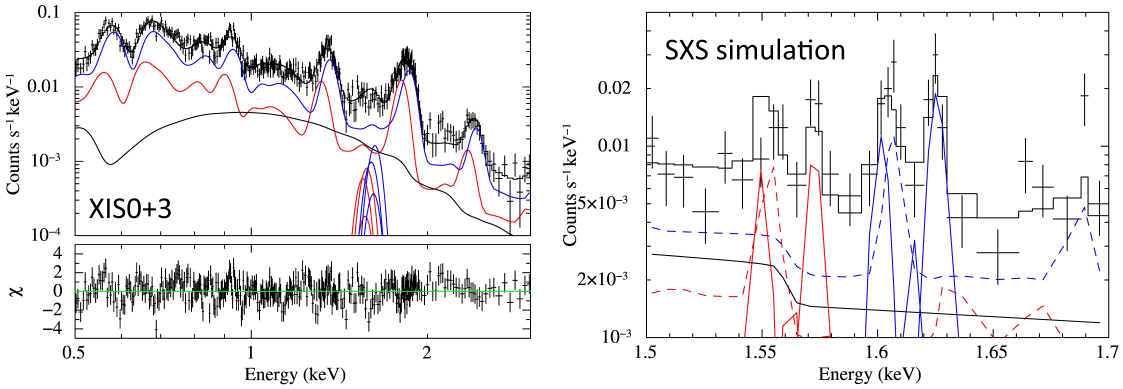

Figure 6: *(Left) Suzaku* XIS spectra extracted from a 3′ × 3′ region near the center of SN 1006 showing the two-component spectral model fit needed to account for the approaching (blue) and receding (red) hemispheres of the SNR. *(Right)* SXS simulation of the best fit XIS model highlighting the region about the Al lines (the Heα resonance and forbidden lines are shown). This simulation assumed a 200 ks exposure with *ASTRO-H*.

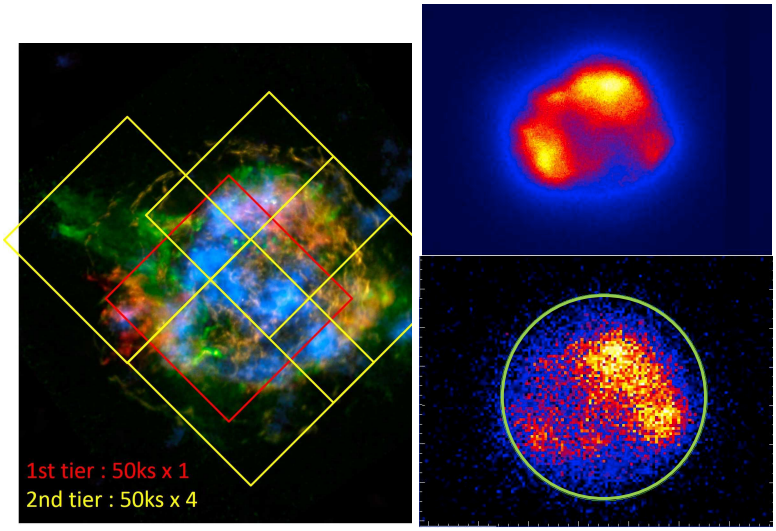

Figure 7: *(Left) Chandra* ACIS (red: Fe; green: Si/Mg) and *NuSTAR* (blue: ^{44}Ti; Grefensette et al. 2014) image of Cassiopeia A with 5 SXS pointings overlaid covering the full SNR. The red box shows a top priority pointing for odd-z measurement. *(Right) sim-x* simulations of Cassiopeia A for the SXI (top) and HXI (bottom). Both simulations use the *Chandra* ACIS image: the 0.7–7 keV band for the SXI simulated image and the 4–7 keV band for the HXI image.

many years indicates that this CCO is a neutron star with a carbon atmosphere whose surface temperature is declining with time (Heinke & Ho, 2010). It has been proposed that this decline is due to neutrino emission from Cooper pair formation as the neutrons in the core become superfluid (Shternin et al., 2011). However, recent *NuSTAR* observations of Cassiopeia A (Grefenstette et al., 2014) led to the interesting suggestion that Cas A's neutron star may have experienced a transition to a quark star by undergoing a second explosion a few days after the supernova itself (Laming, 2014; Ouyed et al., 2014).

The complete explosive burning of Si to ^{56}Ni also forms trace quantities of the radioactive isotope ^{44}Ti. Cas A is the only SNR for which decay lines from both steps in the decay of ^{44}Ti to ^{44}Sc to ^{44}Ca have been unambiguously detected (Iyudin et al., 1994; Vink et al., 2001). The recent 1.2 Ms *NuSTAR* study has *imaged* Cassiopeia A in the light of the ^{44}Ti radioactive decay line at 67.9 keV (Grefenstette et al., 2014), revealing a clumpy, centrally-located distribution that does not correlate well with the X-ray emitting Fe-K shell emission (Hughes et al., 2000b; Hwang et al., 2004). This is a surprising result given the presence of highly pure Fe X-ray emitting clumps (Hwang & Laming, 2003) that were likely formed by complete Si burning and would be expected to also display radioactive ^{44}Ti lines. Recently, Cr K-shell line emission has been detected from Cassiopeia A using *Chandra* (Yang et al., 2009) and *Suzaku* (Maeda et al., 2009). However Mn K-shell lines have not been detected yet.

Figure 7 (left panel) shows five pointings that will allow a complete coverage of Cassiopeia A with the SXS. The central pointing's primary objective is to address the odd-Z elements measurement, providing key information on the nucleosynthesis in this core-collapse remnant. In particular, phosphorus (P), predominantly formed in the O-rich layer, is a very useful diagnostic as it doesn't suffer absorption nor contamination by the Fe-L shell lines. These pointings have been also targeted on the Fe-rich regions at the SE and N rims and the spectrally hard (synchrotron-dominated) region to the SW. In the right two panels of Figure 7, we show simulated SXS and HXI images. For all Cassiopeia A simulations we will require 50 ks for each pointing for a total of 300 ks on-source exposure.

For the SXS spectral simulations, our model closely follows that of Rutherford et al. (2013), which is derived from *Chandra* HETG data. We include bulk-motion line broadening determined from the *Suzaku* XIS. Figure 8 (left panel) shows the energy band containing the strong He-like transitions of Al around 1.6 keV for the combined total 300 ks exposure. The 10 eV broadening assumed in the simulation corresponds to a velocity broadening of ~2000 km s^{-1}. For illustrative purposes we show the spectrum including the Al component as

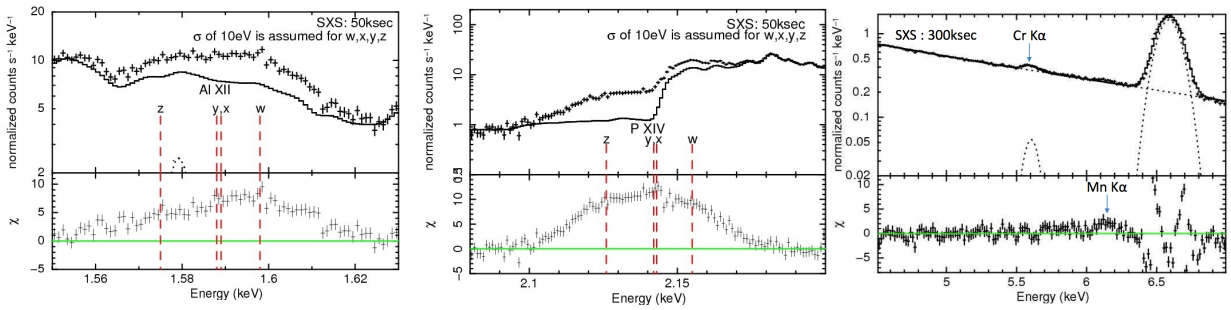

Figure 8: *(Left)* Simulated SXS spectrum of Cassiopeia A from a 50 ks observation showing a close-up of the band containing the He-like w, x, y, z lines of Al (an odd-Z element). *(Middle)* Same as the left panel but for P (an odd-Z element formed in O-rich layer). *(Right)* Simulated 300 ks SXS spectrum of Cassiopeia A showing the band encompassing the Cr, Mn and Fe-K shell lines.

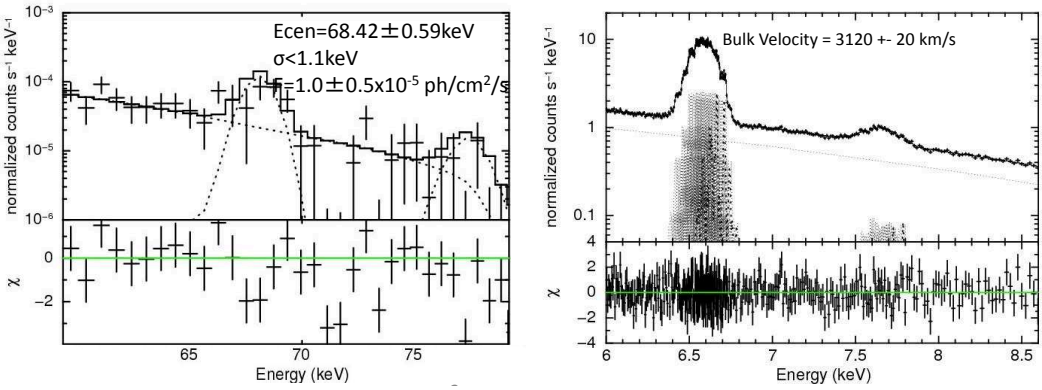

Figure 9: *(Left)* Simulated HXI spectrum of Cassiopeia A from a 300 ks observation. *(Right)* Simulated 100 ks SXS spectrum of the nothern region pointing of Cassiopeia A showing the band encompassing the Fe-Kα and Fe-Kβ lines.

the data points and the spectrum without Al as the solid histogram. The Al lines account for up to 30% of the total flux in this band and will therefore be detected with high significance. As well, in the middle panel of Figure 8 , we highlight the simulated emission from P around 2.15 keV. Being the brightest thermal X-ray supernova remnant, Cassiopeia A is the best target to search for and study the low abundance odd-Z elements, especially from a core-collapse explosion.

The right panel of Figure 8 shows the energy band containing Cr, Mn, and Fe emission and, as above, assumes the total combined exposure of 300 ks. The Fe and Cr lines are well detected, but Mn will be detected only if the Mn to Cr intensity ratio is >0.22, which is about in the midpoint of measured values to date (see Table above). These simulations assumed a conservative velocity broadening of 3000 km s^{-1}. We may have higher sensitivity to Cr and Mn emission by restricting the analysis to regions near the rim where the shocked material will be moving transverse to our line of sight, reducing the bulk-motion velocity broadening.

For the HXI spectral simulations, we assume the *NuSTAR* measured line centers and fluxes (Grefenstette et al., 2014) and a velocity broadening of 3000 km s^{-1}. Figure 9 (left panel) shows the resulting HXI spectrum for a 300 ks exposure. We will be able to detect the ^{44}Ti radioactive decay lines, but to improve on the *NuSTAR* results a much deeper exposure will be required. It may be possible to build up a deeper exposure over the course of the *ASTRO-H* mission.

1.3.4 SN1987A: the youngest known supernova remnant

Chandra and *XMM-Newton* continue to monitor SN1987A as it transitions into a supernova remnant. The coverage with *Chandra* is roughly twice a year for typically 50 ks of exposure and, since 2009, have been carried out with the HETG inserted as a pile-up mitigation strategy. Recent *Chandra* observations (Helder et al., 2013) show the object to be still barely resolved (diameter of ~1.5″) with X-ray fluxes of $F_X = 7.6 \times 10^{-12}$ erg s^{-1} cm^{-2} (0.5–2 keV band) and $F_X = 8.9 \times 10^{-13}$ erg s^{-1} cm^{-2} (3–8 keV band). These fluxes continue to increase at a rate of about 13% per year. Deep observations with the ACIS/HETG (Dewey et al., 2012) in 2007 and 2011 (exposure durations of ~350 ks and ~200 ks) were fitted with a complex multi-parameter three-shock model that included some line broadening (width of 9300 ± 2000 km s^{-1}). The HETG data have good signal-to-noise over the 0.6-2.2 keV band and clearly show emission lines of O VIII, Ne IX and X, Mg XI and XII, and Si XIII and XIV, in addition to the forest of Fe-L lines.

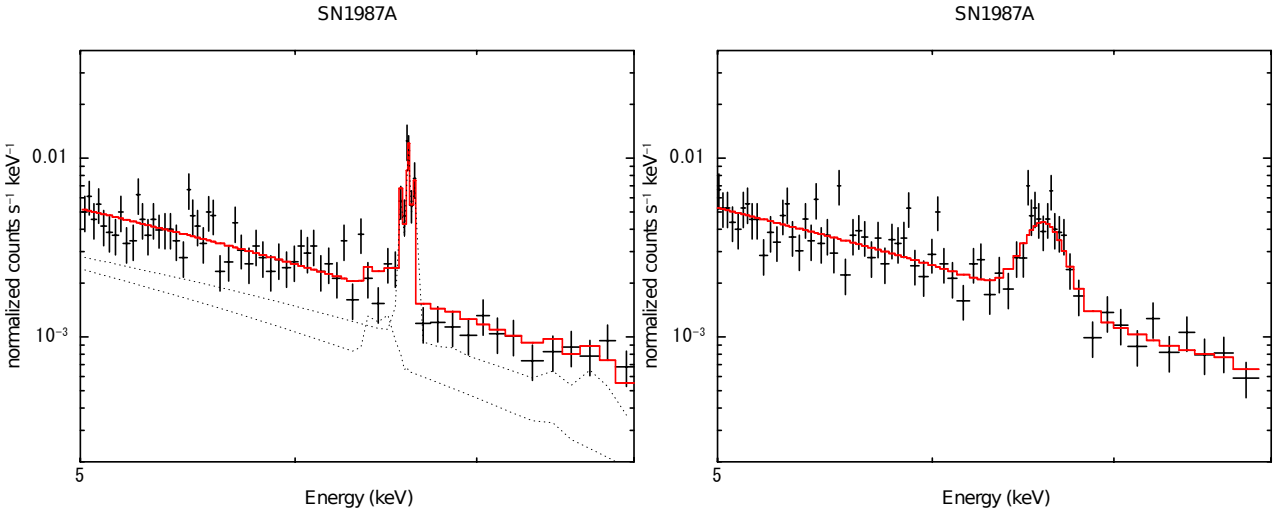

Figure 10: SXS simulations of the Fe-K band of SN1987A for two different cases: a mixture of plasmas with different ionization timescales *(left panel)* and a very broad line component with a FWHM of order 10^4 km s^{-1} *(right panel)*. This simulation assumes an equivalent width of 300 eV for the Fe line.

While the *Chandra*/HETG and *XMM-Newton*/RGS have already revealed emission line structures in SN1987A over the soft X-ray band, the *ASTRO-H* SXS will allow us to perform Fe-K line diagnostics in the higher energy band. Fe-K lines are sensitive to the hottest thermal component and thus to the fastest shocks propagating now

at this early stage of the remnant's evolution. A series of *XMM-Newton*/EPIC spectra from 2007 to 2011 detected a Fe-K line blend (Maggi et al., 2012). The line width was apparently broad, which has been interpreted as being due to a mixture of plasmas with different ionization timescales, possibly including fluorescence and/or low ionization Fe (Maggi et al., 2012). On the other hand, *Chandra*/HETG observations show a very broad line component with a FWHM of order 10^4 km s^{-1} and indicate that most of the 3–10 keV emission would originate from it (Dewey et al., 2012). If this is the case, Fe-K lines should be intrinsically broad. Figure 10 shows the SXS simulations of the two cases. With the *ASTRO-H* SXS, we can clearly distinguish between these two scenarios.

1.3.5 Radioactive species in the youngest Galactic remnant: SNR G1.9+0.1

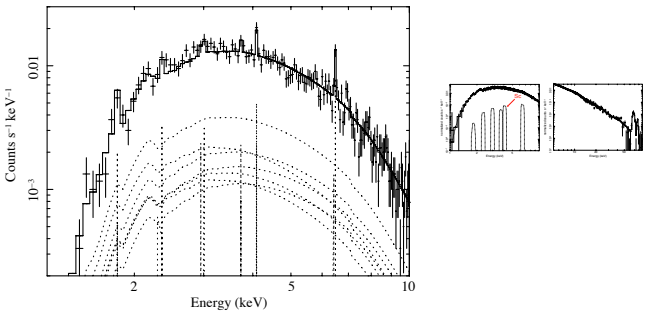

Figure 11: *(Left)* A simulated 100-ks *ASTRO-H* SXS spectrum of G1.9+0.1 *assuming no bulk motion velocity broadening* shows a clear detection of the 4.1 keV Sc line from the radioactive decay of ^{44}Ti. The Fe-K line is clearly detected too. *(Middle)* A simulated 300-ks *ASTRO-H* SXS spectrum of G1.9+0.1 now including the line broadening expected from the remnant's rapid expansion (bulk motion of the ejecta at a speed of ∼14,000 km s^{-1}). No lines are detected above the remnant's strong non-thermal synchrotron continuum emission. *(Right)* The HXI spectrum shows a significant detection of the ^{44}Ti radioactive hard X-ray lines.

G1.9+0.3 is the youngest known Galactic SNR and is located near the center of the Milky Way. The age was originally estimated to be of the order of 100 years (Reynolds et al., 2008); additional strong support for the remnant's youth was provided by *Chandra* measurements of a rapid expansion rate (Carlton et al., 2011). The angular expansion rate of 0.642% ± 0.049% corresponds to a shock velocity of about 13,000 km s^{-1} (assuming a 8.5 kpc distance, as indicated by the SNR's high absorbing column density) consist with the spectroscopically deduced velocities of order 14,000 km s^{-1} (Borkowski et al., 2010). The SNR shows a shell-like morphology with strong synchrotron emission (Reynolds et al., 2009). A deep observation by *Chandra* successfully separated a thermal-dominated region from the strong non-thermal shells (Borkowski et al., 2010). The spectrum exhibits emission lines from low-ionization states of Si, S, Ar, Ca, and Fe, suggesting that it is evolving in a low-density environment. In addition, the ^{44}Sc emission at 4.1 keV, produced by electron capture from ^{44}Ti, was clearly detected. For the remnant age of 100 yr, the measured line strength indicates synthesis of $(1-7)\times10^{-5}$ $M_\odot$ of ^{44}Ti. Although this is in the range predicted for both Type Ia and core-collapse SNe, it is significantly smaller than that reported for Cas A (2×10^{-4} $M_\odot$).

Although the *Chandra* detection of the 4.1 keV line was significant, the statistical uncertainty on the flux was large: the 95% confidence range is $(0.35, 2.4)\times10^{-6}$ ph cm^{-2} s^{-1}. One reason is that the Sc-Kα emission was not clearly resolved from the nearby Ca-Kα line at 3.9 keV. If we ignore any line broadening then the *ASTRO-H* SXS can detect this line even though the non-thermal emission cannot be resolved spatially. Figure 11 (left panel) shows a simulated SXS spectrum of G1.9+0.3 with an exposure of 100 ksec. The 4.1 keV line counts at a rate of $(2.8\pm1.2)\times10^{-4}$ s^{-1}. Refining the ^{44}Ti mass estimate will help determine the SNR's origin (i.e., Type Ia or core-collapse), which remains uncertain.

However, considering the remnant's extremely rapid expansion rate (Borkowski et al. 2013), line broadening from bulk motion will likely render any emission lines undetectable (see Figure 11 middle panel) even in a much deeper (300 ks) observation. *Chandra* was able to detect these lines by isolating the thermal emission spatially from the strong non-thermal rims, which *ASTRO-H* cannot do.

The HXI can make a significant detection of the radioactive decay lines of ^{44}Ti under the plausible assumptions that the synthesized mass of ^{44}Ti is 3.3×10^{-5} $M_\odot$ and the remnant's age is 100 yr. Whether this remains an interesting *ASTRO-H* project depends on the results from the *NuSTAR* observations carried out for this remnant.

1.3.6 Kes 73: a core-collapse remnant associated with an anomalous X-ray pulsar (magnetar)

SNR Kes 73 is a relatively bright and young SNR that hosts the young anomalous X-ray pulsar AXP 1E 1841−045. The remnant is ejecta-dominated, showing strong line emission from Mg, Si and S whose relative abundances make a plausible case for the SNR arising from a very massive progenitor. Kes 73 has an angular size (∼4′ diameter) that is well matched to the *ASTRO-H* field of view.

A recent *Chandra* and *XMM-Newton* study of Kes73 (Kumar et al., 2014) shows that the 0.5–10 keV emission is characterized by two components: a soft component with a temperature kT_s of ∼0.5 keV and a high ionization timescale, a hard component with a temperature kT_h of ≥1.6 keV and a low ionization timescale, and a total luminosity of $\sim 3 \times 10^{37}$ ergs s^{-1} (0.5–10 keV, at an assumed distance of 8.5 kpc). The soft and hard components are attributed to shock-heated ejecta and ISM/CSM, respectively. The age estimated from the properties of the SNR is ≤2.6 kyr (depending on the phase of evolution and the environment in which the SNR is expanding), a factor of ≥2 lower than the pulsar's characteristic age (of 4.7 kyr) which represents an upper limit, indicating a young SNR. The SNR's spectrum clearly shows line emission from Mg, Si, and S with enhanced abundances associated with the soft component, indicating that the SNR is dominated by shock-heated ejecta. The abundances inferred from fitting the global (and spatially resolved spectra) suggest a very massive (≥20 $M_\odot$) progenitor. The abundances were however poorly constrained, and no line emission was detected from O and Fe-K, both needed to better constrain the progenitor's mass.

Figs. 12 and 13 illustrate the sensitivity of the SXS to the line emission from several elements including Mg, Si, S, Ar, Ca and Fe which will provide much better constraints on their abundances and thus the progenitor mass. In particular, SXS will allow the detection of a strong Fe-K line.

Ideally, with two 100 ksec pointings (Figure 12, left), SXS will cover the eastern and western sides of the SNR, including the ejecta-dominated regions and the bright western limb, with the AXP close the edge of the SXS's field of view. Alternatively, a pointing towards the western part will cover the bulk of X-ray emission and the brighter western limb, with the AXP closer to the field's center. Since SXS does not have the spatial resolution needed to resolve the PSR from the SNR emission, the pulsar's spectrum (known in quiescence) will be subtracted from the total source spectrum (addressed in the HMXB+Magnetars White Paper #4). The right panel of Figure 12 shows the simulated SXS 100 ks spectra (of the western field versus the AXP) illustrating the strong line emission from the SNR which dominates the emission from the AXP. We note that the SNR will be fully covered by SXI due to its larger field of view.

Fig 13 (left panel) shows a *sim-x* simulated 100 ks SXS spectrum of the western field with the two-component model, and with the AXP's spectrum excluded. In such an observation the ejecta abundances can be measured to ∼10% (depending on the species), and compared to nucleosynthesis models to confirm or refute the very massive progenitor origin.

Another primary goal of the observation is to confirm the blast wave velocity which has been estimated from CCD spectra to be ∼1200 km s^{-1} (Kumar et al., 2014), with the estimated velocity depending on the SNR's evolutionary phase and the ambient medium in which it's expanding (e.g. expansion into the late red supergiant wind phase of its massive progenitor will yield a higher velocity than expansion into a homogenous ISM). This can be addressed by examining the Fe-Kα line (associated with the hot component) which is easily visible in the SXS data, but barely detected in existing CCD data. Fig 13 (right panel) shows that a 1200 km/s velocity will correspond to a Doppler shifted line detectable in a 100 ksec exposure with the SXS. The velocity estimate will also help constrain the SNR's age and thus address the factor of ≥2 discrepancy between the SNR and pulsar ages. This will in turn address the question of magnetic field decay in magnetars. The AXP's science and simulated broadband spectrum (with HXI and SGD) are discussed in detail in White Paper #4. In summary, the study of this young magnetar-SNR system will take full advantage of *ASTRO-H*'s broadband capability and SXS's spectral resolution, to address fundamental questions related to the formation of magnetars and their link to the other classes of compact objects in core-collapse SNRs.

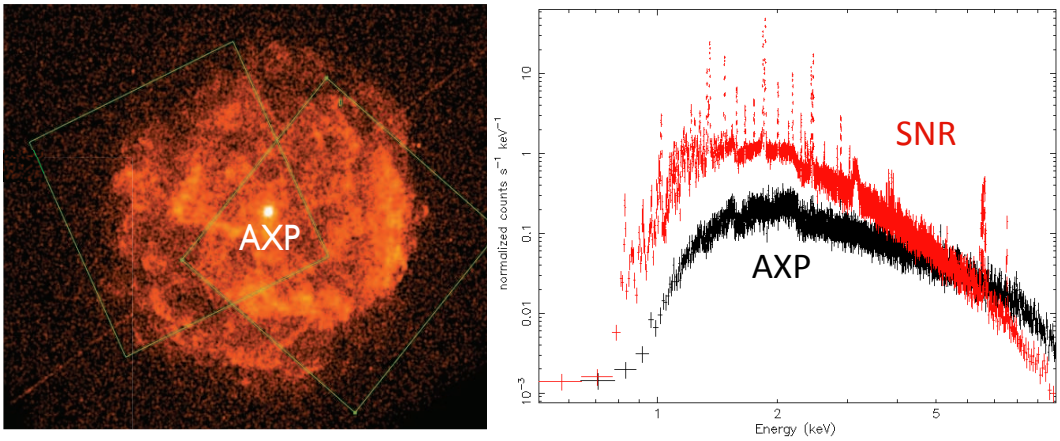

Figure 12: *(Left)* The *Chandra* image of the SNR Kes 73 with the SXS field of view overlaid. The two fields shown cover the eastern and western parts of the SNR with the AXP towards the edge of SXS to minimize contamination of the SNR signal. *(Right)* 100 ks SXS simulation with *sim-x* of the western field showing the relative contributions of the AXP and SNR emission. The line emission from the SNR clearly dominates over the emission from the AXP. The AXP's emission will dominate in the hard band (HXI+SGD).

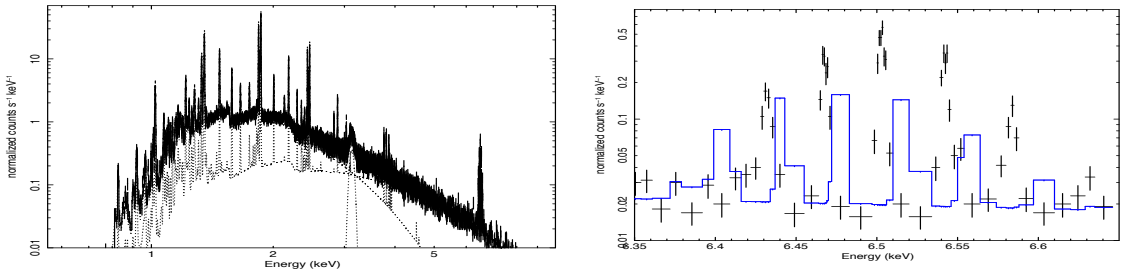

Figure 13: (Left): A 100 ksec SXS simulated spectrum of the SNR emission (excluding the pulsar's emission) using *sim-x* and based on the *XMM-Newton* and *Chandra* spectral fits. The model components are shown as dashed lines (an absorbed two-component thermal model plus a Gaussian line to account for Argon) and correspond to the best fit for the CCD-type spectra. In addition to the power of SXS to constrain the abundances, particularly of Mg, Si, and S in the soft X-ray band, a strong Fe-K line associated with the hot component will be detected. (Right): Zoomed-in SXS simulated spectra of the Fe-K line region, with no Doppler shift, and with the model (blue line) corresponding to a thermal non-equilibrium ionization *pshock* model with a Doppler shift corresponding to an inferred shock shock velocity of ~1200 km s^{-1}.

1.3.7 Other *ASTRO-H* targets

Other targets (young to middle-aged SNRs) worth exploring with *ASTRO-H* to address the science questions raised in this section include the following SNRs, the study of which is relevant to other core-collapse SNRs investigated in detail in this White Paper and in the Pulsar Wind Nebulae section of WP#8:
(a) Kes 75 is associated with HBP J1846?0258, long thought to be a rotation-powered pulsar, but, having been caught once revealing itself as a magnetar, now blurs the distinction between the rotation-powered pulsars and magnetars (Kumar & Safi-Harb, 2008; Gavriil et al., 2008; Ng et al., 2008). Kes 75 has been proposed to be also associated with a very massive, Wolf-Rayet type, progenitor (Morton et al., 2007). *ASTRO-H* will allow a precise determination of abundances for the progenitor mass estimate.
(b) G292.0+1.8, an O-rich remnant like Cas A, but older and harbouring a rotation-powered (more 'normal') pulsar powering a pulsar wind nebula. This is a unique remnant, likely originating from an asymmetric explosion, and showing evidence for interaction of ejecta fragments and the blast wave with a CSM produced by a very massive progenitor's stellar winds (Hughes et al., 2001; Gonzalez & Safi-Harb, 2003; Park et al., 2007). Recent *Suzaku* observations allowed the first detection of hot ejecta through Fe-K shell line emission at 6.6 keV (Kamitsukasa et al., 2014). *ASTRO-H* will allow precise abundance measurements for confirming the progenitor mass estimate. Section 2 further elaborates on the science that can be further addressed with velocity structure measurements (particularly for Mg, Si, S, and Fe-K).
(c) MSH 15–52, a middle-aged core-collapse SNR powered by the high-magnetic field, rotation-powered, pulsar PSR B1509-58. Surrounded by a bright pulsar wind nebula prominent in the hard X-ray band (recently observed with *NuSTAR*, An et al. (2014), and referred to as the "Hand of God"), the pulsar/PWN have been suggested to be interacting with the surrounding medium or SNR shell (e.g. through precessing jets) forming the RCW 89 nebula; see e.g. Yatsu et al. (2005). The emission from this nebula peaks in the soft X-ray band and is an excellent target for *ASTRO-H* SXS for a precise measurement of the velocity distribution, and thus to

confirm or refute the a precessing jet or blast wave origin.
(d) 3C 397, a bright SNR with an unusual morphology, over-abundance in Fe-peaked elements, and whose nature as a type Ia or core-collapse SNR is still being debated (Chen et al., 1999; Safi-Harb et al., 2000, 2005; Yamaguchi et al., 2014). *ASTRO-H* will allow precise determination of abundances, leading to a certain determination of the progenitor type and mass, as well as the search for Cr and Mn lines. In relation to Section 2 below, the study of the velocity structure of the ejecta (particularly Fe) will help probe the explosion mechanism.
(e) SN 1987A: As one of the youngest known and best probed SNRs outside our Galaxy (see Section 1.3.4 for details and Fe-K line diagnostics), SN 1987A's progenitor mass estimate can be used to calibrate progenitor mass estimates of other SNRs. Studying the progenitor type can be achieved through a precise measurement of the abundances and probing the ionization states of Si, S and Fe.

1.4 Beyond Feasibility

Search for the characteristic X-rays from ^{44}Sc in Cas A

Initial SXS simulations for measuring the characteristic line at 4.1 keV from ^{44}Sc (a daughter product of the decay of ^{44}Ti) in Cassiopeia A suggested that only an upper limit was possible in 100 ks. This simulation, however, assumed the radioactive Ti was distributed over the entire SNR and the line was broadened by bulk motion at the expansion speed of the ejecta. *NuSTAR*'s localization of the ^{44}Ti hard X-ray emission lines to the center of Cassiopeia A moving with the expansion speed of the unshocked ejecta, motivates a new look at the detection feasibility. Clearly a central pointing would be required. Successful detection of ^{44}Sc would valid the decay chain and allow for constraints or measurements of the expansion velocity of the radioactive Ti, which cannot be obtained in any other way. This would provide a rare insight into the inner workings of the core-collapse explosion mechanism.

On the possible non-detection of Mn

The single-degenerate scenario has a requirement that the progenitor's metallicity must be higher than $\sim$ 0.1 solar. Otherwise a white dwarf cannot eject over-accreted matter (from its companion) via a radiation-driven stellar wind, and hence the progenitor system undergoes a common-envelope phase (so stable burning of the white dwarf is no longer expected) before the white dwarf obtains the Chandrasekhar mass (Hachisu et al. 1996). Thus, if we find a Type Ia SNR with a metallicity lower than this threshold, this will be direct evidence of its double-degenerate origin. At the moment, there is no plausible candidate of such a type Ia SNR, because even the Small Magellanic Cloud has an average metallicity of $\sim$ 0.15 solar (Russell & Dopita 1992). However, local inhomogeneities in the ISM abundances may allow some SNR progenitors' metallicity to be lower than the mean value of its host galaxy. We should therefore keep in mind that non-detection of the Mn line is important to constraining the progenitor type.

2 Ejecta Distribution in Space and Velocity

2.1 Background and Previous Studies

The questions to be addressed here are twofold: (1) How are the ejecta distributed in core-collapse and SN Ia remnants? (2) What does this tell us about the explosion mechanisms and the physics of shocks in these objects?

Measurement of the distribution of the ejecta in space and velocity provides unique information about both the progenitor star and the details of the explosion. The ejecta from core-collapse SNe and deflagration/detonation (Type Ia) SNe have distinct abundance patterns. Specifically, the ejecta from core-collapse SNe have high ratios compared with cosmic abundances of oxygen to iron; those from Type Ia's have the opposite. X-rays are the ideal band for seeking this signature, as broad band X-ray spectrometers cover the K lines from oxygen and iron, as well as the iron L band. The complications of abundance determination make SN typing challenging. Compounding the difficulty is our inability to know what fraction of the ejecta is visible in the

X-ray band, and the fact that the oxygen abundance is difficult to determine in an unambiguous way as the oxygen line strength correlates with the column density in spectral fitting in moderate spectral resolution detectors. This is particularly problematic for Galactic SNRs with heavy interstellar absorption.

Despite these difficulties, there were some notable early successes in measuring abundances, and deriving physical information from the measurement. The most successful early attempt was the use of *Einstein* FPCS observations of Puppis A to show an overabundance of oxygen with respect to iron, requiring the progenitor to have a mass of more than 25 $M_{\odot}$ (Canizares & Winkler, 1981). Other early observations of note are comprehensive analysis of Tycho data requiring ejecta (Hamilton et al., 1986) and the analysis of an *EXOSAT* observation of W49B requiring the presence of a substantial amount of shocked ejecta (Smith et al., 1985). However, it is with the advent of spatially resolved spectroscopy through which shock structures can be isolated that most of the advances have taken place in our knowledge of the abundances of reverse shocked ejecta and forward shocked ISM. *ASCA* was the pathfinder mission in this regard (e.g., Holt et al. 1994; Hughes et al. 1995), but *XMM-Newton* and *Chandra* excel in these studies. The recent studies are providing real insight into the ejecta masses and their degree of mixing, as well as the explosion mechanism (Vink 2012).

Type Ia Remnants: The two most thoroughly studied Type Ia remnants are Tycho and SN 1006. The *XMM-Newton* image of Tycho shows that the Fe-K emission peaks at a smaller radius than the Fe L emission, verifying that the temperature with the ejecta increases toward the reverse shock (Decourchelle et al., 2001). The narrow band Si image corresponds well with the radio image, and is thought to mark the contact discontinuity, distorted by Rayleigh-Taylor instabilities. This latter conclusion is reinforced in a dramatic fashion by the *Chandra* image of the Si emission, which shows plume like structures throughout the interior (Hwang et al., 2002; Warren et al., 2005), whose structure is reproduced by 3-D hydrodynamic modeling of the ejecta (Warren & Blondin, 2013). Some of the plumes viewed tangentially reach the outer shock.

The line emission in SN 1006 has been a secondary consideration to the non-thermal emission arising from the bright limbs. Line emission is clearly observed throughout the remnant, except in the bright non-thermal limbs. Along the northwestern rim, *Chandra* imaging spectroscopy shows a clear separation between the forward-shocked material and the ejecta (Long et al., 2003). The forward shock shows material at ordinary solar abundances, shock-heated to electron temperatures of ~0.6–0.7 keV. Interior to both the non-thermal northeast shock and the thermal northwest shocks are plume-like structures similar to those observed in Tycho. Their presence invites the speculation that such structure is common in Type Ia remnants. Spectral analysis of these structures reveals enhanced O, Mg, Si, and Fe abundances. No quantitative X-ray based analysis of the ejecta mass has been performed for SN 1006. Abundance measurements in SN 1006 using X-rays are compromised by the known presence of a substantial amount of high-velocity, unshocked ejecta (Fe, Si, S, and O) interior to the reverse shock (Wu et al., 1983).

In addition to these prominent examples, there are a number of other young Type Ia remnants accessible for study using *ASTRO-H*. These include the Galactic remnants Kepler, G1.9+0.1, and RCW 86, and the LMC remnants 0509, 0519, and N103B.

Core-Collapse SNRs: Core-collapse SNRs generally exhibit highly inhomogeneous ejecta in X-rays (e.g., Hughes et al. 2000b; Hwang et al. 2004; Park et al. 2007). SXS measurements of the radial velocities of different elements as a function of position provides a three-dimensional picture of the ejecta dynamics needed to distinguish between various explosion scenarios. For example, jet-like models can be distinguished from models involving hydrodynamic instabilities based on their velocity maps. By measuring the abundances of the ejecta produced near the mass cut, SXS also provides insight into the core-collapse that initiates the explosion.

The first *Chandra* images revealed clear and unexpected differences in the distribution of metals (e.g., Hughes et al. 2000b; Hwang et al. 2000a). The Si, S, Ar, and Ca maps are similar to each other, and to the distribution of fast optical knots. Equivalent width maps reveal the distribution of the prominent ejecta constituents. The structures in these maps contrast sharply with the 0.5–10.0 keV broadband map and the 4–6 keV continuum map. The northeastern jet, known from optical studies to contain Si group ejecta, shows up strongly in these maps. The Fe-K emission has a very different morphology. In particular, in the southeast of the remnant, the Fe-K emission is located at larger radii than the Si. This suggests that the inner Fe ejecta layers have been overturned and propelled beyond the Si group ejecta in this part of the remnant (Figure 7). Such overturning is

consistent with recent models of core-collapse explosions (e. g., Burrows, Hayes, & Fryxell 1995). Willingale et al. (2002) have used the *XMM-Newton* imaging data to infer the global metal abundance ratios and compare them with supernova models. They show that the ratios with respect to Si of a large number of lines is most consistent with the theoretical nucleosynthesis yield for a 12 $M_{\odot}$ progenitor.

Detailed studies of individual knots show that they have a variety of compositions. Features with distinct composition can be found on the smallest size scales. While most knots show a mix of ejecta, some are dominated by Si group elements and others by Fe. At least one knot emits Fe lines exclusively, and apparently is devoid of lower mass material. The knots also show a variety of ionization conditions, which have been used in the context of analytic hydrodynamical models to constrain the ejecta density profile, the location of the knots in mass coordinates, and the degree of explosion asymmetry (Laming & Hwang, 2003; Hwang & Laming, 2003). The ejecta show a range of density profiles, from very shallow ($\propto r^n$, where n~6) to very steep, (n~30–50). The ejecta close to the jet show the shallowest profile, possibly due to an asymmetric explosion in which more of the energy is directed along the jet than elsewhere. For a total ejecta mass of 2 $M_{\odot}$ expected from a 20 $M_{\odot}$ progenitor, the Fe-rich clumps are found to arise in a layer 0.7–0.8 $M_{\odot}$ from the center. The observed composition appears to be possible only if Si burning products are mixed with O burning products.

The overall appearance of Cas A contrasts starkly with the young Type Ia remnants. Cas A consists of small knots and thin filaments, not the emission plumes observed in Tycho. The similarity between the structures in Cas A and the prediction of models involving Fe bubbles has been noted. Laming & Hwang (2003) argue that the knots are not especially over-dense compared with their surroundings, and their high ionization ages and the proximity of some to the forward shock are the result of early passage through the reverse shock.

The *Chandra* image of the other O-rich and young (~1600 yr) SNR G292.0+1.8, reveals a thin, nearly circular outer shell of hard emission filled with an array of knots and filaments rivalling Cas A in complexity and contrasting starkly with the Type Ia remnants (Hughes et al., 2001; Park et al., 2002; Gonzalez & Safi-Harb, 2003). The composition and distribution of the shocked ejecta are different from Cas A. The ejecta consist primarily of O, Ne, and Si, with less S and Ar, and very little Fe (although a recent *Suzaku* study led to the detection of hot Fe ejecta; Kamitsukasa et al. 2014) , and are distributed primarily around the remnant's periphery. An X-ray bright equatorial band has normal composition, and is thought to be associated with pre-supernova mass loss (e.g. Park et al. 2007). Measuring the velocity structure of the ejecta could be addressed *ASTRO-H* (see also Section 1.3.7).

Compared with the Type Ia remnants there is a dearth of young or historical Galactic core-collapse remnants. As with the Type Ia remnants, however, the *ASTRO-H* sample can be expanded through the study of bright Magellanic Cloud remnants, including 1E 0102.2−7219 and N63A.

2.2 Prospects & Strategy

Specific questions that *ASTRO-H* can provide unique information about include: (i.) what is the large-scale velocity structure and metal abundance spatial distribution of SN ejecta; (ii.) how much turbulent velocity structure is there; (iii.) what are the ion temperatures in the ejecta and how do they compare to the thermal, bulk, and turbulent velocities; i.e., can we distinguish between the different constituents of a SNR (e.g., ejecta, ISM) using velocity or line width information; (iv.) can we detect evidence for radioactive decay of short-lived isotopes the lines of ^{44}Ti, its daughter product ^{44}Sc (4.1 keV) or Co-K (6.9 keV); (v.) can we detect evidence for supra-thermal electrons to address the injection problem in particle acceleration at shocks?

All of the above questions can be addressed using the high resolution, spatially-resolved spectroscopy enabled by the SXS and/or the broad band imaging spectroscopy provided by the HXI. The SXS allows us to: measure the velocity structure, abundances and spatial distribution of SN ejecta; measure thermal, bulk, and turbulent velocities in resolved ejecta features; search for weak lines from radioactive decay products; and use Fe-K diagnostics and line shapes for to search for supra-thermal electrons. The HXI allows a measurement of the hard continuum to search for non-thermal Bremsstrahlung from supra-thermal electrons, and should provide sufficient sensitivity at the high end of its band to detect the ^{44}Ti lines at 68 and 78 keV in some remnants.

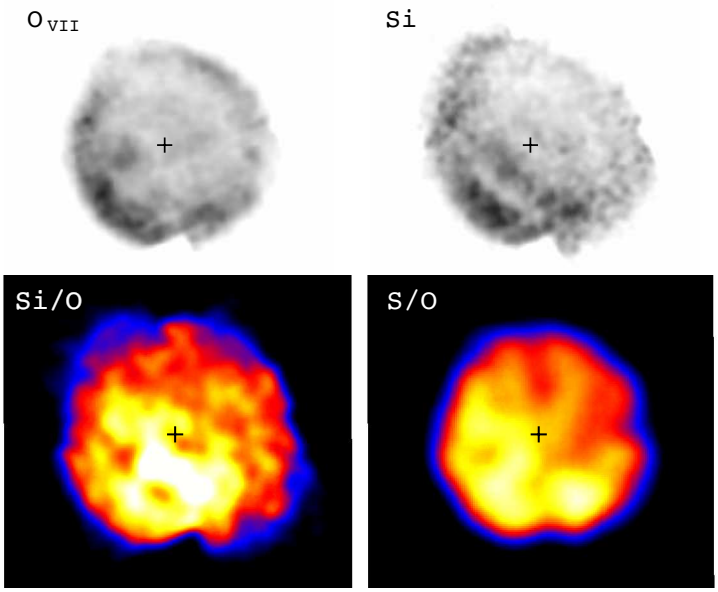

Figure 14: *Suzaku* XIS images of SN 1006 in the O (top-left) and Si (top-right) bands. Equivalent-width-ratio images of Si/O and S/O are shown in bottom-left and bottom-right, respectively (Uchida et al. 2013). These indicate asymmetric distribution of the intermediate-mass elements.

2.2.1 Structural diversity in Ia remnants

Type Ia SNe are important astronomical phenomena because of their use for a study of cosmology; the large and relatively homogeneous luminosity make them to be standardizable candles to measure cosmological distance, which contributed to revealing the accelerating universe (Riess et al., 1998; Perlmutter et al., 1999) The SNe Ia also made an important role in chemical evolution of the universe, as they are major sources of Fe-peak elements (e.g., Nomoto et al. 1984). Despite effort in the last decades, however, detailed explosion mechanism of SNe Ia is still unsolved. It is widely known that type Ia SNe show diversity in their optical spectra and lightcurve (e.g., Phillips et al. 1999; Benetti et al. 2005). A primary origin of the diversity is under the debate. One interpretation is that spherically asymmetric explosion is primarily responsible (e.g., Kasen et al. 2009). Maeda et al. (2010a) systematically studied SNe Ia and found that random viewing angles for such asymmetric (but almost identical) explosions can quantitatively explain the observed spectral diversity. Besides them, recent multi-dimensional simulations have suggested that thermonuclear ignition in Type Ia progenitors is offset from their center (e.g., Woosley et al. 2004; Kuhlen et al. 2006). If this interpretation is the case, a SNR should show nonuniform ejecta distribution as the result. Some observations of SNRs in X-rays indeed revealed such asymmetric distribution of ejecta. Figure 14 shows *Suzaku*/XIS narrow-band images of SN 1006 (Uchida et al., 2013). Si and other intermediate-mass elements concentrate in the southeast region, while the lighter elements (i.e., O, Ne, Mg) distribute relatively homogeneously. Tycho also shows evidence of local inhomogeneity in the ejecta (e.g., Vancura et al. 1995).

There is, however, another interpretation for the major origin of the diversity. Mazzali et al. (2007) showed that the summed masses of ^{56}Fe and the intermediate-mass elements are almost uniform among various SNe Ia, even though the ^{56}Fe mass is widely spattered in the range of $0.2\,M_{\odot}$–$0.9\,M_{\odot}$. They thus argued that the diversity mainly originates from the difference in explosion energy and/or density when a deflagration-to-detonation transition (DDT) occurs (see Section 1). Theoretically, both the explosion energy or DDT density affect the expansion velocity of the SN ejecta (e.g., Iwamoto et al. 1999), which can be investigated by high-resolution spectra of SXS.

Investigation into global distribution and velocity structure of ejecta is also important to understand how the explosive nucleosynthesis wave propagates in the exploding white dwarf. A delayed-detonation scenario,

well accepted as a standard SN Ia model, predicts layered composition of nucleosynthesis products with little effect of mixing (e.g., Maeda et al. 2010b). On the other hand, a full deflagration explosion predicts significant mixing among the elements (e.g., Röpke et al. 2007). X-ray observations of Ia SNRs show evidence of layered ejecta distribution with Fe commonly concentrated toward the SNR's center with respect to the lighter high-abundance elements, such as Si and S (e.g., Hwang & Gotthelf 1997), supporting qualitatively the delayed-detonation scenario. However, the distribution among other elements (e.g., Si vs Cr, Cr vs Fe, Fe vs Ni) are still unknown. How does DDT occur? Recent multi-dimensional simulations showed that a deflagration-dominant SN Ia produces larger turbulent instabilities than detonation-dominant one (e.g., Kasen et al. 2009), suggesting that dimmer SNe Ia should have larger velocity dispersion in their ejecta. Howell et al. (2001) showed that sub-luminous SNe Ia are more spherically asymmetric than luminous ones. These would be important subjects for high-resolution observations with SXS.

So far, distribution of ejecta in SNRs has been investigated mostly by X-ray images. This is, of course, the most straightforward way. The high-resolution imaging capability of *Chandra* and *XMM-Newton* has largely improved our knowledge of spatial structure in SNRs during this decade. Unfortunately, the angular resolution of *ASTRO-H* is not as good as that of *Chandra* or *XMM-Newton*. We can, however, still investigate global ejecta distribution with a different way, making most use of the capability of SXS. Given that a SNR's reverse shock heats and ionizes the ejecta from the outer layer inward, the inner ejecta should have a lower ionization age than the outer ejecta. In fact, Fe ejecta in Tycho and SN 1006 are known to have a lower ionization age compared to the intermediate-mass elements (Hwang & Gotthelf, 1997; Yamaguchi et al., 2008). In addition, recent *Suzaku* observations of Tycho with deep exposure has revealed that Fe-Kβ emission has a smaller peak radius than the Fe-Kα emission (Yamaguchi et al. 2013; Figure 1). Since the Kβ emission is induced by $3p \rightarrow 1s$ transition following $1s$-shell ionization, this is likely to originate from the more-recently-shocked ejecta with extremely low ionization state ($Fe^{\sim 8+}$; see also the New Spectral Features White Paper #17), showing clearly the correlation between the radius and ionization age. With high-resolution spectra of SXS, we can more accurately measure an ionization age of **each independent element** from the line centroid or ratio of their emission (which is also essential to determine accurate abundance; Section 1).

As mentioned above, it was suggested that dimmer SNe Ia tend to have a larger velocity dispersion (Kasen et al., 2009). We can explore the correlation between the Fe abundance and turbulence velocity of several SNRs. This can also be done with the SXS. The SXI also help investigate large-scale ejecta asymmetry.

2.2.2 SN 1006: An exceptional target

Here we describe how these measurements provide insight into some of the key questions using SN 1006 as an example. SN 1006 is an exceptionally important target for *ASTRO-H*. It is the remnant of the brightest supernova ever observed, a Type Ia explosion. In contrast, today its remnant is under-luminous at all wavelengths, due to its location in a very low ambient density high above the Galactic plane. Its distance is reasonably well determined to be 2.2 kpc, and its ~30-arcminute extent makes it well suited for spatially resolved spectroscopy. While its emission is dominated by bright bands of non-thermal emission in its NE and SW quadrants, the X-rays from the interior arise from reverse shocked ejecta, characteristic of a Type Ia remnant. The proper motion in the NE and NW filaments has been directly measured using *Chandra* observations at 5000 and 3000 km s^{-1}, respectively.

Wu et al. (1983) detected high velocity, UV absorption lines from low ionization states of Fe and Si using IUE observations of the Schweitzer-Middleditch (SM) star that lies close to the center of SN 1006 in projection. This has provided invaluable information on the properties of the *unshocked* ejecta in SN 1006. With the SXS on *ASTRO-H* we can measure the velocity structure of the *shocked* ejecta along very nearly the same line-of-sight.

SN 1006 has a reported measurement of an ion temperature based on X-ray data compared to an optically determined velocity. In the X-ray, Vink et al. (2003) used the RGS on *XMM-Newton* to measure the widths of the O VII and VIII K-shell lines coming from a knot on the northwestern edge. The width they measured, $\sigma = 3.4 \pm 0.5$ eV, indicates an oxygen temperature of $kT \sim 500$ keV. This temperature, if assumed to arise from the thermalization of the shock velocity according to the Rankine-Hugoniot relations, $kT_i = (3/16) m_i v_s^2$, implies

a shock velocity of ~4000 km s^{-1}, broadly consistent with the value from optical studies. The main weakness of this result is the assumption that turbulent velocities are negligible (i.e., the observed line broadening is purely thermal). This concern can be addressed by the *ASTRO-H* SXS by studying the line widths across different elemental species.

SN 1006's integrated X-ray spectrum is dominated by non-thermal synchrotron emission from relativistic electrons with energies approaching the TeV range (Koyama et al., 1995). But this emission only comes from two bright "caps" located on the northeast and southwest rims of the remnant. As shown by Cassam-Chenaï et al. (2008), the southeastern rim shows very faint radio emission and no non-thermal X-rays based on *Chandra* observations. Cassam-Chenaï et al. (2008) make the case for azimuthal variation of the efficiency of CR acceleration around the rim of SN 1006: minimum in the SE and maximum in the NE and SW bright lobes. Although there is no evidence for non-thermal emission from the southeast (and northwest rims), the emission there appears to be entirely from shock-heated ejecta (e.g., Katsuda et al. 2013). Thus it is clear that there is significant variation in the density of relativistic (non-Maxwellian) electrons around the rim of SN 1006. This difference provides a unique opportunity to search for the effects of a non-Maxwellian electron distribution on the emission line properties.

SN 1006 observations can therefore be used to address many of the questions of interest:

1. Identifying lines present in the X-ray spectrum, and using them to determine the abundances and state of the plasma across the remnant (temperature, degree of equilibrium), as discussed in detail in Section 1 above.

2. Measuring the expansion velocity along the line of sight by separation of red and blue shifted components. Measuring the velocity along the rims through line broadening. In principle it will be possible to search for velocity differences among the individual elements (e.g., O vs. Si). Combining the expansion measurement with the X-ray proper motions already determined by *Chandra* will provide an independent measurement of the distance to SN 1006. This will not be subject to uncertainties in the interpretation of the widths of optical Balmer lines, as the current most precise distance measurements are.

3. Determining the electron-ion temperature non-equilibration at various locations along the rim. It will be possible to search for differences in ion temperatures among distinct ionization states and elements.

4. Detecting the effects of non-thermal particles on thermal emission: This could manifest itself in one of two ways: either the lines are narrower than expected given the velocity, due to energy leakage into cosmic-rays (e.g., Hughes et al. 2000a; Helder et al. 2009), or the lines are broader than expected due to atomic interactions with accelerated ions (Tatisheff et al., 1998).

2.3 Targets & Feasibility

Many of these questions will be addressed by observing the same targets as mentioned in Section 1 above. We present next specific feasibility estimates for two illustrative targets: SN 1006 and the LMC SNR 0519–69.0.

2.3.1 SN 1006: determining the expansion velocity in multiple elemental species

For SN 1006 *ASTRO-H* SXS simulations were performed for the center, NW rim and NE rim, based on emission models derived from fitting *Chandra* ACIS and *Suzaku* XIS data. The inferred count rates for these regions are 0.11, 0.09, and 0.31 cts/s for the center, NW rim (outer half of the FOV), and the NE rim, respectively.

The center field spectrum included expansion velocities of +6000 km s^{-1} (redshift) and -5000 km s^{-1} (blueshift) for O, and +5000 km s^{-1} (redshift) and -4000 km s^{-1} (blueshift) for Si (see Figure 15). An exposure time of 200 ks gives fairly tight constraints: ±3% for O Heα and ±10% for Si Heα. In reality, multiple-ionization plasma along the line of sight may cause some additional uncertainties.

Thermal Doppler broadening was introduced into the NW rim and center spectra by adding thermal width to the lines of σ = 2.4 eV (Vink et al., 2003). This width is clearly resolved in the 200 ks exposure of the center and a 100 ks exposure of the NW rim.

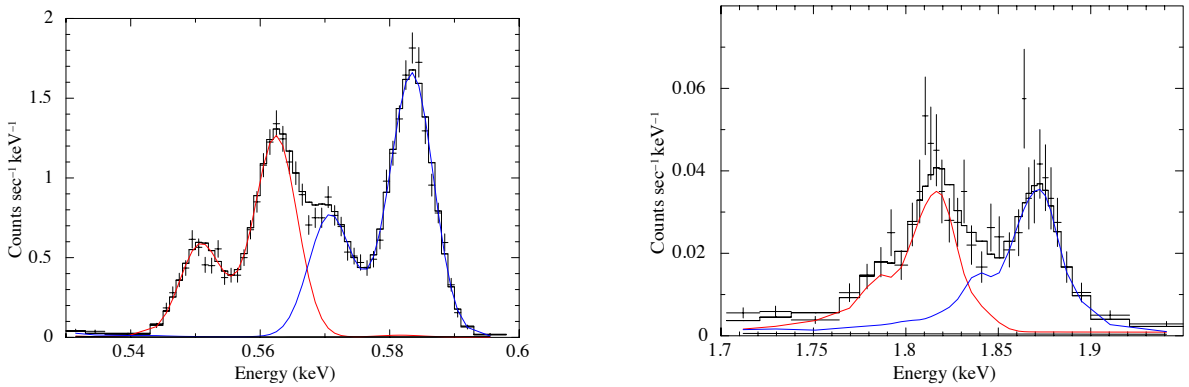

(a) Oxygen (b) Silicon

Figure 15: Simulated SXS observations of a pointing near the center of SN 1006 showing Oxygen (*Left*) and Silicon (*Right*) that demonstrates how cleanly we will be able to separate the emission from the approaching (blue curves) and receding (red curves) hemispheres of the expanding shell of ejecta.

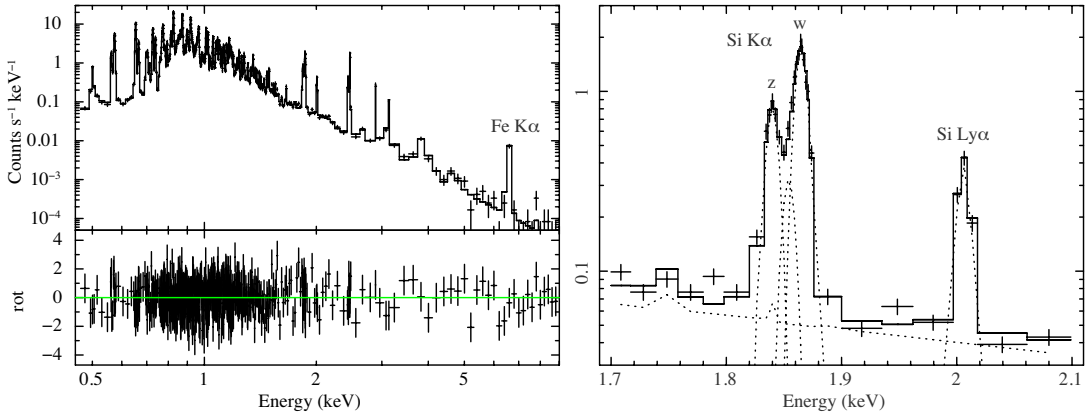

Figure 16: Simulated SXS spectrum of SNR 0519–69.0 with an exposure of 60 ksec. The widths of Si lines can be determined with an error of ~10%.

2.3.2 SNR 0519–69.0: bulk motion expansion

SNR 0519–69.0 is the second brightest (in soft X-rays) LMC remnant of Type Ia SN origin. In the optical band this remnant shows a pure Balmer line spectrum (Tuohy et al., 1982) with a broad Hα component width of 2800 ± 300 km s^{-1}. Similarly broad H Lyβ was detected in FUSE observations, which were used to constrain the velocity of the forward shock to be 2600–4500 km s^{-1} (Ghavamian et al., 2007). The RGS spectrum (Rasmussen et al., 2002) shows broadened X-ray lines, likely due to the expansion velocity of the shell. Figure 16 shows a simulated SXS spectrum of SNR 0519–69.0 for a 60 ksec exposure, assuming a bulk motion velocity broadening consistent with previous work. The widths of Si lines can be determined with an uncertainty of ~10%.

2.3.3 Other *ASTRO-H* targets

Many of the questions discussed in this section will be addressed by observing the following SNRs: Tycho, SN 1006, Cas A, SN 1987A, G1.9+0.1. Additional targets include Kepler, RCW 86, G292.0+1.8, 0509−67.5, 0519−69.0, and N63A.

Furthermore, SN 1987A (see Section 1.3.4) is a promising target for this science topic, particularly for measuring the velocity structure of Mg, Si, S and Fe lines. Multiple pointings spanning several years will allow

us to track the time variability of all emission components, and further address the topics discussed in Sections 1 and 3 as well.

2.4 Beyond Feasibility

The radial velocity structure of Cas A from the profile of the Fe-K line

For this "Beyond Feasibility" section we reach back to the Cassiopeia A simulation presented in Section 1.3.3. The general idea is to use a specific line profile to inform the radial velocity structure of that particular species. It can be applied to any emission line from any remnant, but Cas A's exceptional brightness makes it the best case on which to attempt such a measurement.

Figure 9 (right panel) shows the detailed structure of the line emission from different charge states contributing to the Fe K line for an NEI model that matches the *Suzaku* Cassiopeia A observation. The expected bulk motion of 3000 km s^{-1}, included in the full spectrum that is plotted above the individual line contributions, smears out the charge state structure. With some assumptions (e.g., that the thermodynamic state does not vary strongly with radius) and sufficient signal, it may be possible to extract information on the radial velocity distribution from the Fe-K line profile. Arriving at a robust result from this measurement will be challenging.

3 How Does the Thermal Plasma State of a Supernova Remnant Link with the Efficiency of its Particle Acceleration?

3.1 Background and Previous Studies

Key questions to address in this topic area are: Where is the thermal emission in synchrotron-dominated SNRs?; what is the partition of shock energy into bulk motions, thermal energy, and relativistic particles?

Supernova remnants have long been considered to be the primary acceleration sites of cosmic-ray particles below the energy of the so-called *knee* in the cosmic ray spectrum, $\sim 10^{15}$ eV. The first evidence for multi-TeV acceleration was the discovery of synchrotron X-ray emission from the shell of the supernova remnant SN 1006 (Koyama et al., 1995). Recent high quality morphological and spectral studies with the HESS TeV imager combined with the X-ray imager such as *ASCA*, found a good keV-TeV correlation from RX J1713.7−3946 (Aharonian et al., 2004) and RXJ 0852.0−4622 (Aharonian et al., 2007), indicating that both the X-rays and the TeV γ-rays are emitted by the TeV particles in the SNR shell. The extremely thin X-ray filaments with a 0.02 pc width in SN 1006 (Bamba et al., 2003; Long et al., 2003), as well as the X-ray variability on time scales of a year from RX J1713.7−3946 (Uchiyama et al., 2007) strongly support the efficient acceleration of particles by SNR shocks. Up to now, many observational results support that supernova remnants (SNRs) are major sources of galactic TeV cosmic rays.

Efficient acceleration of cosmic rays (CR) at a supernova shock has several observational consequences. First is the increase in the compression factor above the typical factor of four assuming the Rankine-Huguniot jump conditions. This has the effect of modifying the structure of the shocked region, particularly the gap between the forward shock and the contact discontinuity (Decourchelle et al., 2000), an effect that has now been observed in both Tycho (Warren et al., 2005) and SN 1006 (Cassam-Chenaï et al., 2008; Miceli, 2012). Directly imaging the gap requires the high angular resolution of *Chandra*, but the increased density enhances the ionization state of the post-shock gas (Patnaude et al., 2009) and may therefore be observable by the *ASTRO-H* SXS.

Furthermore, recent 3D hydrodynamical simulations coupled with a non-linear acceleration model to account for efficient particle acceleration show that the integrated thermal X-ray emission is reduced with particle back-reaction, with the effect being more significant for the highest photon energies (e.g. Fe-K vs. O-K to Ne-K energy band) (Ferrand et al., 2012). As well, the computed non-thermal emission maps and broadband spectra (radio, X-rays and γ-rays) can be used to probe the presence of energetic *ions* at the shock (Ferrand et al., 2014) since, in addition to impacting the dynamics of the shock and thermal X-ray emission (as mentioned above), they impact the evolution of the magnetic field and thus the non-thermal emission from electrons. High magnetic fields (>100μG) directly impact the synchrotron emission from electrons, by restricting their

emission to thin rims, and indirectly impact the inverse Compton emission from electrons and the pion decay emission from protons by shifting their cut-off energies to respectively lower and higher energies. Such high magnetic fields have been in fact inferred from X-ray observations of non-thermal rims of bright and young SNRs such as Tycho (e.g., Slane et al. 2014) and of synchrotron-dominated, efficient particle accelerators, such as RX J1713.1−3946 (Uchiyama et al., 2007). For RX J0852.0–4622 (Vela Junior), however, the level of magnetic field amplification remains an open question (Lee et al., 2013; Aharonian et al., 2007; Berezhko et al., 2009; Bamba et al., 2005). Such effects can be observed with *ASTRO-H* SXS and HXI+SGD observations, combined with high-resolution (*Chandra* or *XMM-Newton*) observations and multi wavelengths studies from radio to TeV energies.

The level to which we can observe such effects strongly depends on the efficiency of CR acceleration at the supernova shock. This efficiency can be as high as 50% (e.g. Morlino et al. 2013; Helder et al. 2009), which represents a sizeable drain of energy from the thermal population. In this case the temperature of the ions and electrons will be reduced with a measurable effect. In particular, for SNRs with accurately known shock velocities (like those in the Magellanic Clouds or with shock velocities determined from broad Balmer lines) it will be possible to combine shock velocity measurements with temperature measurements to search for evidence of a reduced temperature due to efficient particle acceleration. This was done early on during the *Chandra* mission for the young oxygen-rich SNR 1E 0102.2−7219 (Hughes et al., 2000a), where a significantly lower electron temperature was measured compared to the shock velocity (lower even when non-equipartition of electron-ion temperatures was included).

Another related topic concerns the lack of thermal X-ray emission from the synchrotron-dominated shell-type SNRs, e.g., RX J1713.7−3946 and RX J0852.0−4622, for which CR acceleration efficiency is believed to be high. The *ASTRO-H* SXS should take deep exposures near the non-thermal rims of these SNRs to detect or set the best constraint on the thermal emission. Detecting a thermal signature will be a major discovery since it will provide an estimate for the ambient medium density and thus allow us to confirm or refute the hadronic vs. leptonic origin of their TeV γ-ray emission.

We also wish to highlight the injection mechanism of cosmic ray electrons. Electrons that enter into diffusive shock acceleration must be pre-accelerated to supra-thermal energies (above ∼10 keV) to cross the shock front. We currently do not understand how these energies are attained. The observational constraint of the energy spectrum of supra-thermal electrons will bring critical information on the injection mechanism.

3.2 Prospects & Strategy

In order to carry out a study of the loss of shock energy to relativistic particles at the expense of the thermal particles, we require "clean" shocks where the thermal emission is clearly from the post-shock flow (and not further back or from a different component like the ejecta when studying the forward shock). The best possible strategy for this involves observing a large Galactic remnant with well studied Balmer shocks. SN 1006 may not be ideal, because of its strong ejecta emission and lack of X-ray emission from its interstellar forward shock. RCW 86 may be the best candidate.

To address the injection problem, we have two approaches to detect supra-thermal electrons at the early stage of the acceleration process: plasma diagnostics by high-resolution spectra with SXS and hard X-ray mapping with HXI.

With the SXS, we can resolve the He-like triplet and Li-like satellite lines. The He-like resonance line "w" is sensitive to both thermal and supra-thermal population, while the dielectronic recombination (DR) satellite lines such as "j" and "d13" are only sensitive to discrete energies in thermal domain (Gabriel & Phillips, 1979). For thermal plasma, the line ratios "d13"/"j" and "w/j" are determined only by the temperature. If supra-thermal electrons exist, however, the ratio "w/j" is enhanced. The excess of "w/j" above purely thermal case gives the quantitative constraint to the energy spectrum of supra-thermal electrons. This method is originally proposed and succeeded for solar flares (Gabriel & Phillips, 1979; Seely et al., 1987). The similar idea using H-like resonance and the He-like satellite lines is also proposed for cluster plasma (Kaastra et al., 2009).

Hard X-ray imaging spectroscopy with HXI can also put constraints on the supra-thermal distribution of

electrons. In solar flares, hard X-ray bursts have been observed preceding the rise of supra-thermal electrons (Seely et al., 1987). Such direct bremsstrahlung would be detected from SNR shocks well above the cut-off energy of synchrotron X-rays. While past hard X-ray observations were not able to bring significant results (Kalemci et al., 2006; Vink, 2008), a deep observation with the superior imaging capability of HXI may detect the emission for the first time. Mapping the bremsstrahlung emission from supra-thermal electrons would reveal their spatial distribution behind the shocks, which gives additional information on the injection mechanism.

3.3 Targets & Feasibility

3.3.1 Cas A: non-thermal X-ray emission

Cas A is one of several SNRs from which non-thermal X-rays and TeV γ-rays have both been detected (X-rays: Allen et al. 1997; Uchiyama & Aharonian 2008, TeV: Aharonian et al. 2001; Albert et al. 2007). In X-rays Cassiopeia A seems to consist of a number of thermal and non-thermal X-ray emitting knots/filaments (Hughes et al., 2000b; Hwang et al., 2004; Bamba et al., 2005). Although some non-thermal emission is associated with the forward shock, the dominant source of non-thermal emission may be identified with the reverse shock regions (Helder & Vink, 2008; Maeda et al., 2009). It therefore is a unique object in which we can study the particle acceleration by the reverse shock, because for the other SNRs the acceleration seems to originate from the forward shock region only (e.g., Parizot et al. 2006).

A long observation of Cas A will be gradually made over several years. Such a long-term observation gives us a bonus to make a flux and spectral shape monitor of the synchrotron emission from the non-thermal high energy electrons. Patnaude et al. (2011) showed that the soft X-ray continuum of Cas A has declined between 2000 and 2010. At the same time the spectrum has softened. This can be understood assuming a loss-limited synchrotron spectrum, as the exponential cut-off energy depends solely on the braking of the shock velocity. This is a reasonable interpretation, but should be clarified with a follow-up observation since the spectral slope and flux is also dependent on an assumption of the limit (age or loss) and evolution of magnetic field, etc. (see Vink 2012). Above ~8 keV, the X-ray flux is dominated by the synchrotron emission (c.f., Maeda et al. 2009). The wide band spectroscopy with the HXI and the SXI covers a band above the cut-off energy at possibly ~3 keV (c.f., Maeda et al. 2009) up to ~80 keV. The band is very sensitive to test if the cut-off origin fully explain the spectra slope and flux seen in *Chandra*.

Cas A is also a plausible target for searching for supra-thermal electrons. The remnant has both the bright radio emission from energetic electrons and strong K-shell lines from highly ionized Fe ions. As the reverse shock is responsible for the accelerated particles as well as the metal-rich plasma in Cas A (Helder & Vink, 2008), the interaction between the supra-thermal electrons and Fe ions is naturally expected.

3.3.2 RX J1713.1–3946: the search for thermal line emission

The primary goal of an *ASTRO-H* observation of this powerful cosmic ray accelerator is to detect the expected thermal line emission from the hot post-shock plasma, which has not been detected previously. In the absence of a thermal component we are left without many useful diagnostic tools to characterize the shock properties (i.e., ambient medium density, temperatures, ionization timescales). The high resolution spectral capabilities of the SXS will allow the line emission to stand out above the strong non-thermal continuum. Two "big picture" science questions that we aim to address are: (1) what is the ambient density – this gets at the interpretation of the TeV gamma-ray emission (leptonic vs. hadronic) and (2) what is the thermal pressure behind the shock – which gets at the fraction of shock energy going into thermal and relativistic particles.

Given the large size of this remnant (~1° in diameter), the obvious question is where to point the SXS. The NW rim is an attractive option because it is one of the X-ray brightest regions (see *Suzaku* XIS contours on the H.E.S.S. image in the left panel of Figure 18), it is where the twinkling X-ray filaments are (Uchiyama et al., 2007), there are radio filaments in the vicinity, and it is close to a molecular cloud (Slane et al., 1999).

This SNR has been extensively studied with *XMM-Newton* (Cassam-Chenaï et al., 2004; Hiraga et al., 2005) and *Suzaku* (Takahashi et al., 2008; Tanaka et al., 2008; Sano et al., 2013). We have verified, using these archival

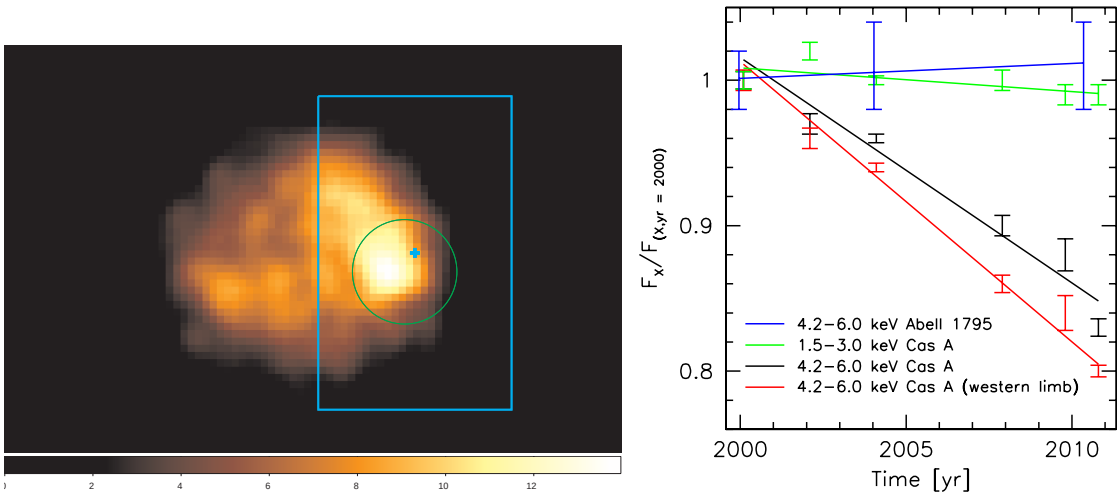

Figure 17: Left: *Suzaku* XIS 8–11 keV band image (Maeda et al. (2009)). The green circle is the region where the continuum emission dominates. Right: Comparison of 4.2–6.0 keV flux in Cassiopeia A compared to the year 2000 observations by Patnaude et al. (2011) using *Chandra*. The black curve and data correspond to changes in the whole SNR, while the red curve and data correspond to changes in the western portion of Cassiopeia A only (Green circle in left figure). For reference, we show the 1.5–3.0 keV flux from Cassiopeia A (fluxed at 1.85 keV) as well as the 4.2–6.0 keV emission from the cluster Abell 1795. The observed decline in the 4.2–6.0 keV emission in Cassiopeia A corresponds to a fractional decline of $-(1.5\pm0.17)\%$ yr^{-1} across the whole SNR, and $-(1.9\pm0.10)\%$ yr^{-1} in the western limb (Patnaude et al., 2011).

data, that the NW region is the best candidate for the thermal emission search. We note that the less absorbed interior would be a good site for the detection of thermal X-ray emission from shock-heated ejecta; however the SXS simulations show that the analysis will be complicated by the contamination from the Galactic ridge X-ray emission and the low-surface brightness of the SNR interior.

We used a *Chandra* observation of the NW rim (ObsId: 12671, 90 ks nominal exposure) to estimate the level of possible thermal contribution to the spectrum. Spectra were extracted from two regions, each the size of the full SXS array (3.05′×3.05′), from one location with bright filamentary emission (NW1) and another with fainter diffuse emission (NW2) as shown in Figure 18 (middle panel). A modified version of the *Chandra* data was made by spreading the detected events around by the point-spread-function (PSF) of the *ASTRO-H* soft X-ray telescope, assumed to be the same for all photon energies. The smoothed image is the right panel of Figure 18. The bright region yielded fewer extracted events (90%) while the faint region produced more events (130%) when using the data set with the simulated PSF of *ASTRO-H*. This level of contamination should not be a concern.

Fits were initially done with a naive model consisting of an absorbed power-law model (`phabs*pow`). For the bright NW1 region the χ^2 of the fit is acceptable (421/463 d.o.f.), although a pattern of low energy residuals was left (see top left panel of Figure 19). Note that similar patterns of low energy residuals are apparent in high signal-to-noise *Suzaku* spectra (Takahashi et al., 2008). Inclusion of a thermal component (single temperature, solar abundance `mekal` model) resulted in a significant reduction of χ^2 (397/461 d.o.f.) for a temperature $kT = 0.21 \pm 0.3$ keV and norm 4.9×10^{-3} (see top right panel of Figure 19). Next we introduced a more conservative model to describe the continuum, the so-called `srcut` model which produces a gently curving spectrum throughout the X-ray band, which is believed to more accurately reflect the underlying physics of the emission. This model by itself does a better job at fitting the continuum than the pure power-law case (407/463 d.o.f.). Again the fit is improved if we include a thermal component and we get essentially the same χ^2 and best-fit temperature as before. However the spectral norm of the `mekal` model is reduced by about a factor of two (norm = 1.8×10^{-3}).

Simulated SXS spectra show prominent lines that stand out above the continuum from O VIII (1s-np series), Ne IX (forbidden, inter-combination, and resonance), Ne X, and the strong 15 Å line blend of Fe XVII (see

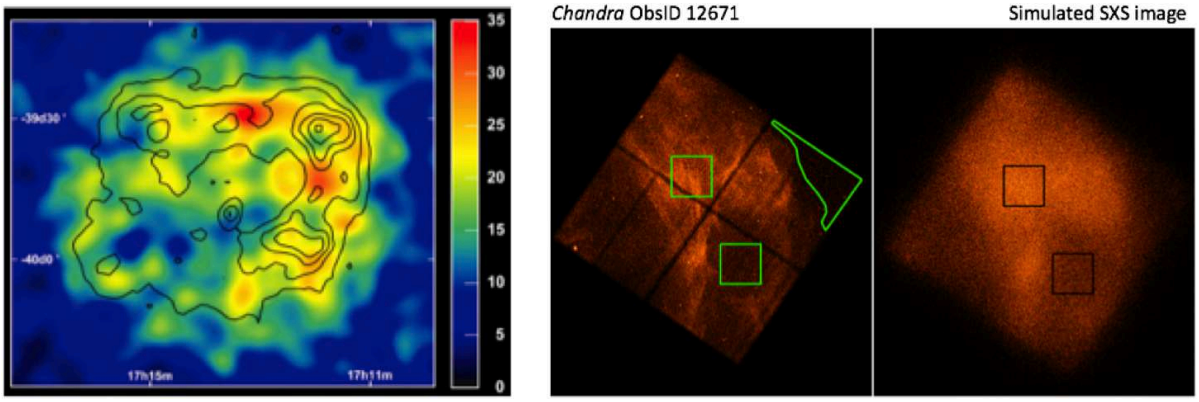

Figure 18: *(Left)* Images of RX J1713.1−3946 from H.E.S.S. and *Suzaku* XIS (contours) (Aharonian et al. 2004). *(Middle) Chandra* observation of the NW rim showing the two regions used to simulate SXS spectra (boxes) and the region used for background. *(Right) Chandra* smoothed to approximate the *ASTRO-H* point-spread-function.

bottom panels in Figure 19). According to our simulations such high signal-to-noise spectra are going to require 100 ks to 300 ks of exposure, assuming that our estimates of the thermal emission inferred from the *Chandra* data accurately describe the true thermal emission from the forward shock in RX J1713.1−3946.

Note that there is strong interest in this target from White Paper #18, the Shock Acceleration task force team. We have not investigated here the constraints on the broadband continuum emission from joint fits to the SXS, SXI, and HXD, since this is addressed in WP#18.

3.3.3 Other *ASTRO-H* targets

Other promising *ASTRO-H* targets for addressing this science topic include RCW 86, RX J0852.0−4622, and SN 1006. For RCW 86, 1–2 *ASTRO-H* pointings at the northeast rim will allow a measurement of the degree of equipartition. Measuring the line widths in that region will determine the effect of non thermal particles. For RX J0852.0−4622 (Vela Junior), *ASTRO-H* pointings at the rim and interior will allow us (like for RX J1713.1−3946) to characterize the properties of the ambient medium (and possibly ejecta) by searching for line emission from this synchrotron-dominated SNR. For SN 1006 which has both thermal and non-thermal X-ray emission, the bright non-thermal limbs, strongly correlated with TeV emission observed with HESS (Acero et al. 2010), will make a good *ASTRO-H* target to address the acceleration efficiency in this Ia SNR, in comparison to the synchrotron-dominated SNRs like RX J1713.1−3946. In addition, mapping the synchrotron-dominated limbs in all these SNRs with HXI will help determine the shape of the electron energy distribution beyond the synchrotron cutoff (of relevance to WP#18).

3.4 Beyond Feasibility

Narrow Fe-K emission lines in Tycho: Evidence for cosmic ray acceleration at the reverse shock

This "Beyond Feasibility" section refers back to the Tycho simulation presented in Section 1.3.1. The reverse shock speed in Tycho can be estimated to be ∼4000 km s^{-1} using the expansion velocity of the Fe-Kα line measured by *Suzaku* (Hayato et al., 2010). With the Rankine-Hugoniot shock jump conditions we derive an ion temperature of $kT_{\rm Fe} = 3/16 M_{\rm Fe} v_{\rm RS}^2 \sim 2\,$MeV. This seems to be the most likely situation for Tycho and, therefore, the simulations presented above included this amount of line broadening. However, if cosmic ray acceleration is efficient at the reverse shock in Tycho, then the ion temperature could be much lower. Therefore, if we detect Fe-K emission lines much narrower than ∼1 MeV, it would suggest that cosmic ray acceleration is efficient at the reverse shock, which would be a major breakthrough in this field.

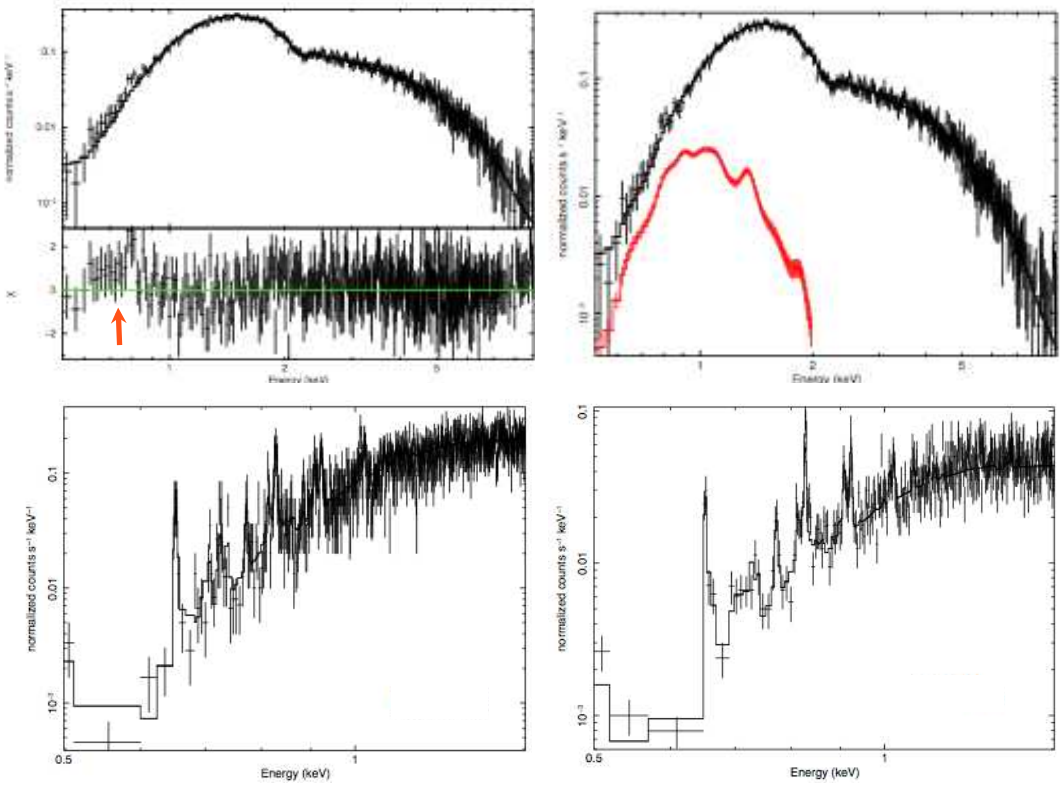

Figure 19: *(Top left) Chandra* spectrum of region NW1 in RX J1713.1−3946 with best fit absorbed power-law fit. *(Top right)* The same spectrum now shown with the best-fit model after the inclusion of an additive `mekal` thermal model. The best fit thermal component is plotted in red. *(Bottom left)* Simulated SXS spectrum of the NW1 region assuming a 100 ks exposure using the best fit absorbed power-law plus `mekal` fit from the *Chandra* data. *(Bottom right)* Simulated SXS spectrum of the fainter NW2 region assuming a 300 ks exposure using the best fit absorbed power-law plus `mekal` fit from the *Chandra* data.

4 Summary

Young SNRs represent the best astrophysical probes for studying a wide range of fundamental questions, from the formation of the chemical elements to the acceleration of cosmic rays to very high energies, to the creation of some of the most exotic objects in the Universe. We have highlighted in this White Paper some of the important topics for young SNR studies that we expect to carry out with *ASTRO-H*, in particular with the SXS that will open a new discovery window to tackle fundamental questions in supernova remnant and cosmic ray astrophysics. We have not stressed here *ASTRO-H*'s broadband capability to be provided with combined SXI, HXI and SGD studies, filling an important energy gap between current X-ray missions and gamma-ray missions; however this important aspect of the *ASTRO-H* mission is addressed in the Acceleration White Paper (#18). As well, the Old SNRs+PWNe White Paper (#8) highlights science topics for older SNRs and Pulsar Wind Nebulae (which would be also relevant to the ISM and new physics), and the Highly Magnetized Neutron Stars White Paper (#4) focuses on their (associated) compact objects' science.

References

Acero, F. et al. 2010, A&A, 516, 62

Aharonian, F., et al. 2001, Astronomy & Astrophyics, 370, 112

Aharonian, F. A., et al. 2004, Nature, 432, 75

Aharonian, F., et al. 2007, ApJ, 661, 236

Albert, J., et al. 2007, Astronomy & Astrophyics, 474, 937

Allen, G. E., et al. 1997, ApJ, 487, L97

An, H. et al. 2014, ApJ, 793, 90

Anders, E., & Grevesse, N. 1989, Geochimica et Cosmochimica Acta 53, 197

Aubourg, É., Tojeiro, R., Jimenez, R., et al. 2008, Astronomy & Astrophyics, 492, 631

Badenes, C., Bravo, E., Borkowski, K. J., & Domínguez, I. 2003, ApJ, 593, 358

Badenes, C., Hughes, J. P., Cassam-Chenaï, G., & Bravo, E. 2008a, ApJ, 680, 1149

Badenes, C., Borkowski, K. J., Hughes, J. P., Hwang, U., & Bravo, E. 2006, ApJ, 645, 1373

Badenes, C., Bravo, E., & Hughes, J. P. 2008b, ApJ, 680, L33

Bamba, A., Yamazaki, R., Ueno, M., & Koyama, K. 2003, ApJ, 589, 827

Bamba, A., Yamazaki, R., Yoshida, T., Terasawa, T., & Koyama, K. 2005, ApJ, 621, 793

Bamba, A., Yamazaki, R., & Hiraga, J. S. 2005, ApJ, 632, 294

Benetti, S., Cappellaro, E., Mazzali, P. A., et al. 2005, ApJ, 623, 1011

Berezhko, E. G., Pühlhofer, G., & Völk, H. J. 2009, A&A, 505, 641

Blondin, J. M., & Mezzacappa, A. 2006, ApJ, 642, 401

Blondin, J. M., Borkowski, K. J., & Reynolds, S. P. 2001, ApJ, 557, 782

Borkowski, K. J., Hendrick, S. P., & Reynolds, S. P. 2006, ApJ, 652, 1259

Borkowski, K. J., Reynolds, S. P., Hwang, U., Green, D. A., Petre, R. et al. 2013, ApJ, 771, L9

Borkowski, K. J., Reynolds, S. P., Green, D. A., et al. 2010, ApJ, 724, L161

Burbidge, E. M., Burbidge, G. R., Fowler, W. A., & Hoyle, F. 1957, Reviews of Modern Physics, 29, 547

Burrows, A., Hayes, J., & Fryxell, B. A. 1995, ApJ, 450, 830

Burrows, A., Dessart, L., Ott, C. D., & Livne, E. 2007, Phys. Rep, 442, 23

Camilo, F., Manchester, R. N., Gaensler, B. M., Lorimer, D. R., & Sarkissian, J. 2002, ApJ, 567, L71

Canizares C. R., & Winkler, P. F. 1981 ApJ, 246, L33

Carlton, A. K., Borkowski, K. J., Reynolds, S. P., et al. 2011, ApJ, 737, L22

Cassam-Chenaï, G., Decourchelle, A., Ballet, J., Sauvageot, J.-L., Dubner, G., & Giacani, E. 2004, A&A, 427, 199

Cassam-Chenaï, G., Hughes, J. P., Ballet, J., & Decourchelle, A. 2007, ApJ, 665, 315

Cassam-Chenaï, G., Hughes, J. P., Reynoso, E. M., Badenes, C., & Moffett, D. 2008, ApJ, 680, 1180

Chen, Y., Sun, M., Wang, Z-R, & Yin, Q. F. 1999, ApJ, 520, 737

Chevalier, R. 2005, ApJ, 619, 839

Chu, Y.-H., & Kennicutt, R. C., Jr. 1988, AJ, 96, 1874

Decourchelle, A, Sauvageot, J. L., Audard, M., Aschenbach, B., Semblay, S., Rothenflug, R., Ballet, J., Stadlbauer, T., & West, R., 2001, A&A, 365, L218

Decourchelle, A, Ellison, D. C., & Ballet, J. 2000, ApJ, 543, L57

Dewey, D., Dwarkadas, V. V., Haberl, F., Sturm, R., & Canizares, C. R. 2012, ApJ, 752, 103

Dwarkadas, V. 2005, ApJ, 630, 892

Ferrand, G., Decourchelle, A. & Safi-Harb, S. 2012, ApJ, 760, 34

Ferrand, G., Decourchelle, A. & Safi-Harb, S. 2014, ApJ, 789, 49

Foglizzo, T., Scheck, L., & Janka, H.-Th. 2006, ApJ, 652, 1436

Gabriel, A. H., & Phillips, K. J. H. 1979, MNRAS, 189, 319

Gaensler, B. M., & Wallace, B. J. 2003, ApJ, 594, 326

Gaensler, B. M., McClure-Griffiths, N. M., Oey, M. S., Haverkorn, M., Dickey, J. M. & Green, A. J. 2005, ApJ, 620, L95

Gavriil, F. et al. 2008, Science, 319, 1802

Ghavamian, P., Blair, W. P., Sankrit, R., Raymond, J. C., & Hughes, J. P. 2007, ApJ, 664, 304

Gonzalez, M., & Safi-Harb, S. 2003, ApJ, 583, L61

Grefenstette, B. W., Harrison, F. A., Boggs, S. E., et al. 2014, Nature, 506, 339

Hachisu, I., Kato, M., & Nomoto, K. 1996, ApJ, 470, L97

Hamilton, A. J. S., Sarazin, C. L., & Szymkowiak, A. E. 1986, ApJ, 300, 713

Hayato, A., Yamaguchi, H., Tamagawa, T., et al. 2010, ApJ, 725, 894

Helder, E. A., & Vink, J. 2008, ApJ, 686, 1094

Helder, E., et al., 2009, Science, 325, 719

Helder, E. A., Broos, P. S., Dewey, D., et al. 2013, ApJ, 764, 11

Heinke, C. O., & Ho, W. C. G. 2010, ApJ, 719, L167

Herant, M., Benz, W., Hix, W. R., Fryer, C. L., & Colgate, S. A. 1994, ApJ, 435, 339

Hiraga, J. S., Uchiyama, Y., Takahashi, T., & Aharonian, F. A. 2005, A&A, 505, 157

Holt, S. S., Gotthelf, E. V., Tsunemi, H., Negoro, H. 1994, PASJ, 46, L151

Howell, D. A., Höflich, P., Wang, L., & Wheeler, J. C. 2001, ApJ, 556, 302

Howell, D. A., Sullivan, M., Brown, E. F., et al. 2009, ApJ, 691, 661

Hughes, J. P., Rakowski, C. E., & Decourchelle, A. 2000a, ApJ, 543, L61

Hughes, J. P., Rakowski, C. E., Burrows, D. N., & Slane, P. O. 2000b, ApJ, 528, L109

Hughes, J. P., Slane, P. O., Burrows, D. et al. 2001, ApJ, 559, L153

Hughes, J. P., Ghavamian, P., Rakowski, C. E., & Slane, P. O. 2003, ApJ, 582, L95

Hughes, J. P., Hayashi, I., Helfand, D., et al. 1995, ApJ, 444, L81

Hughes, J. P., Slane, P. O., Burrows, D. N., et al. 2001, ApJ, 559, L153

Hwang, U., & Gotthelf, E. V. 1997, ApJ, 475, 665

Hwang, U., & Laming, J. M. 2003, ApJ, 597, 362

Hwang, U., Decourchelle, A., Holt, S. S., & Petre, R., 2002, ApJ, 581, 1101

Hwang, U., et al., 2004, ApJ, 615, L117

Hwang, U., Holt, S.S. & Petre, R., 2000a, ApJ, 537, L119

Hwang, U., Petre, R., & Hughes, J. P. 2000b, ApJ, 532, 970

Iwamoto, K., Brachwitz, F., Nomoto, K., et al. 1999, ApJS, 125, 439

Iyudin, A. F., Diehl, R., Bloemen, H., et al. 1994, Astronomy & Astrophyics, 284, L1

Jiang, B., Chen, Y., Wang, J., Su, Y., Zhou, Xin, Safi-Harb, S., & DeLaney, T. 2010, ApJ, 712, 1147

Jordan, G. C., IV, Fisher, R. T., Townsley, D. M., Calder, A. C., Graziani, C., Asida, S., Lamb, D. Q., & Truran, J. W. 2008, ApJ, 681, 1448

Kaastra, J. S., Bykov, A. M., & Werner, N. 2009, Astronomy & Astrophyics, 503, 373

Kamitsukasa, F., Koyama, K., Tsunemi, H. et al. 2014, PASJ, 66, 64

Kalemci, E., Reynolds, S. P., Boggs, S. E., et al. 2006, ApJ, 644, 274

Kasen, D., Röpke, F. K., & Woosley, S. E. 2009, Nature, 460, 869

Katsuda, S., et al. 2013, ApJ, 763, 85

Kifonidis, K., Plewa, T., Janka, H.-T., Müller, E. 2000, ApJ, 531, L123

Khokhlov, A. M., Höflich, P. A., Oran, E. S., Wheeler, J. C., Wang, L., & Chtchelkanova, A. Y. 1999, ApJ, 524, L107

Koyama, K., et al. 1995, Nature, 378, 255

Kuhlen, M., Woosley, S. E., & Glatzmaier, G. A. 2006, ApJ, 640, 407

Kumar, H. S. & Safi-Harb, S. 2008, ApJ, 678, L43

Kumar, H. S., Safi-Harb, Gonzalez, M. E. 2012, ApJ, 754, 96

Kumar, H. S., Safi-Harb, S., Slane, P. O., Gotthelf, E. V. 2014, ApJ, 781, 41

Krause, O., Birkmann, S. M, Usuda, T., et al. 2008, Science, 320, 1195

Krause, O., Tanaka, M., Usuda, T., et al. 2008, Nature, 456, 617

Lopez, L. A., Ramirez-Ruiz, E., Huppenkothen, D., Badenes, C., & Pooley, D. A. 2011, ApJ, 732, 114

Laming, J. M. 2014, Nature, 506, 298

Laming, J. M., & Hwang, U. 2003, ApJ, 597, 347

Lee, J.-J., Park, S., Hughes, J. P., Slane, P. O., & Burrows, D. N. 2011, ApJ, 731, L8

Lee, S.-H., Slane, P. O., Ellison, D. C., Nagataki, S. & Patnaude, D. J. 2013, ApJ, 767, 20

Lewis, K. T., Burrows, D. N., Hughes, J. P., et al. 2003, ApJ, 582, 770

Long, K. S., Reynolds, S. P., Raymond, J. C., Winkler, P. F., Dyer, K. K., & Petre, R. 2003, ApJ, 586, 1162

Maeda, Y., Uchiyama, Y., Bamba, A., et al. 2009, PASJ, 61, 1217

Maeda, K., Benetti, S., Stritzinger, M., et al. 2010a, Nature, 466, 82

Maeda, K., Röpke, F. K., Fink, M., et al. 2010b, ApJ, 712, 624

Maeda, K., Terada, Y., Kasen, D., et al. 2012, ApJ, 760, 54

Maggi, P., Haberl, F., Sturm, R. & Dewey, D. 2012, A&A, 548, 3

Mazzali, P. A., Röpke, F. K., Benetti, S., & Hillebrandt, W. 2007, Science, 315, 825

Mereghetti, S. 2013, Brazilian Journal of Physics, 43, 356 (arXiv:1304.4825)

Miceli, M., Acero, F., Dubner, G., Decourchelle, A., Orlando, S., & Bocchino, F. 2012, ApJ, 782, L33

Morton, T. D. et al. 2007, ApJ, 667, 219

Morlino, G., Blasi, P., Bandiera, R., & Amato, E. 2013, A&A, 558, 25

Murdin, P., & Clark, D. H. 1979, MNRAS, 189, 501

Nagataki, S., Shimizu, T. M., & Sato, K. 1998, ApJ, 495, 413

Nakamura et al. 1999 ApJ, 517, 193

Ng, C. Y. et al. 2008, ApJ, 686, 508

Nomoto, K., Thielemann, F.-K., & Wheeler, J. C. 1984, ApJ, 279, L23

Nomoto, K., Iwamoto, K., Nakasato, N., et al. 1997, Nuclear Physics A, 621, 467

Nomoto, K., Tominaga, N., Umeda, H., Kobayashi, C., & Maeda, K. 2006, Nucl. Phys. A, 777, 424

Ouyed, R., Leahy, D., & Koning, N. 2014, arXiv:1404.5063

Parizot, E., Marcowith, A., Ballet, J., & Gallant, Y. A. 2006, Astronomy & Astrophyics, 453, 387

Park, S., Hughes, J. P., Slane, P. O. et al. 2007, ApJ, 670, L121

Park, S., Badenes, C., Mori, K., et al. 2013, ApJ, 767, L10

Park, S., Hughes, J. P., Burrows, D. N., et al. 2003, ApJ, 598, L95

Park, S., Hughes, J.P., Slane, P.O., Burrows, D.N., Gaensler, B.M., Ghavamian, P. 2007, ApJ, 670, L121

Park, S., Hughes, J. P., Slane, P. O., et al. 2004, ApJ, 602, L33

Park, S., Roming, P. W. A., Hughes, J. P., Slane, P. O., Burrows, D. N., Garmire, G. P., & Nousek, J. A. 2002, ApJ, 564, 39

Patnaude, D. J., Ellison, D. C., & Slane, P. 2009, ApJ, 696, 1956

Patnaude, D. J., et al. 2011 ApJL, 729, L28

Perlmutter, S., Aldering, G., Goldhaber, G., et al. 1999, ApJ, 517, 565

Phillips, M. M., Lira, P., Suntzeff, N. B., et al. 1999, AJ, 118, 1766

Rasmussen, A., Behar, E., & Vink, J. 2002, 34th COSPAR Scientific Assembly, 34,

Rest, A., Matheson, T., Blondin, S., et al. 2008a, ApJ, 680, 1137

Rest, A., Welch, D. L., Suntzeff, N. B., et al. 2008b, ApJ, 681, L81

Reynolds, S. P., Borkowski, K. J., Green, D. A., et al. 2008, ApJ, 680, L41

Reynolds, S. P., Borkowski, K. J., Green, D. A., et al. 2009, ApJ, 695, L149

Reynolds, S. P., Borkowski, K. J., Hwang, U., et al. 2007, ApJ, 668, L135

Riess, A. G., Filippenko, A. V., Challis, P., et al. 1998, AJ, 116, 1009

Röpke, F. K., & Bruckschen, R. 2008, New Journal of Physics, 10, 125009

Röpke F. K., Woosley S. E., Hillebrandt W., 2007, ApJ, 660, 1344

Rosado, M., Ambrocio-Cruz, P., Le Coarer, E., & Marcelin, M. 1996, A&A, 315, 243

Russell, S. C., & Dopita, M. A. 1992, ApJ, 384, 508

Rutherford, J., Dewey, D., Figueroa-Feliciano, E., Heine, S. N. T., Bastien, F. A., Sato, K., & Canizares, C. R. 2013, ApJ, 769, 64

Safi-Harb, S. & Kumar, H. 2013, Proceedings of the International Astronomical Union, 291, 480, ed. J. van Leeuwen (arXiv:1210.5261)

Safi-Harb, S., Petre, R., Arnaud, K. A., Keohane, J. W., Borkowski, K. J., Dyer, K. K., Reynolds, S. P., & Hughes, J. P. 2000, ApJ, 545, 922

Safi-Harb, S., Dubner, G., Petre, R., Holt, S. S., & Durouchoux, P. 2005, ApJ, 618, 321

Sano, H., Tanaka, T., Torii, K. et al. 2013, ApJ, 778, 59

Scannapieco, E., & Bildsten, L. 2005, ApJ, 629, L85

Scheck, L., Janka, H.-Th, Foglizzo, T., & Kifonidis, K. 2008, A&A, 477, 931

Seely, J. F., Feldman, U., & Doschek, G. A. 1987, ApJ, 319, 541

Seward, F. D., Williams, R. M., Chu, Y.-H., Dickel, J. R., Smith, R. C., & Points, S. D. 2006, ApJ, 640, 327

Shternin, P. S., Yakovlev, D. G., Heinke, C. O., Ho, W. C. G., & Patnaude, D. J. 2011, MNRAS, 412, L108

Slane, P., Gaensler, B. M., Dame, T. M., et al. 1999, ApJ, 525, 357

Slane, P. O., Lee, S.-H., Ellison, D. C., Patnaude, D. J., Hughes, J. P. et al. 2014, ApJ, 783, 33

Smith, A., Jones, L. R., Peacock, A., & Pye, J. P., 1985, ApJ, 296, 469

Smith, R. C., Kirshner, R. P., Blair, W. P., & Winkler, P. F. 1991, ApJ, 375, 652

Sullivan, M., Conley, A., Howell, D. A., et al. 2010, MNRAS, 406, 782

Takahashi, T., Tanaka, T., Uchiyama, Y., et al. 2008, PASJ, 60, 131

Tamagawa, T., et al. 2009, PASJ, 61, S155

Tananbaum, H. 1999, IAU Circ., 7246, 1

Tanaka, T., Uchiyama, Y., Aharonian, F. A. et al. 2008, ApJ, 685, 988

Tatischeff, V., Ramaty, R., & Kozlovsky, B. 1998, ApJ, 504, 874

Thielemann, F-K, Nomoto, K, & Hashimoto, M 1996, ApJ, 460, 408

Timmes, F. X., Woosley, S. E., Hartmann, D. H., & Hoffman, R. D. 1996, ApJ, 464, 332

Timmes, F. X., Brown, E. F., & Truran, J. W. 2003, ApJ, 590, L83

Tsujimoto, T., & Shigeyama, T. 2012, ApJ, 760, L38

Tuohy, I. R., Dopita, M. A., Mathewson, D. S., Long, K. S., & Helfand, D. J. 1982, ApJ, 261, 473

Uchida, H., Yamaguchi, H., Koyama, K. 2013, ApJ, 771, 56

Uchiyama, Y., Aharonian, F. A., Tanaka, T., Takahashi, T., & Maeda, Y. 2007, Nature, 449, 576

Uchiyama, Y., & Aharonian, F. A. 2008, ApJ, 677, L105

van der Heyden, K. J., Behar, E., Vink, J., Rasmussen, A. P., Kaastra, J. S., Bleeker, J. A. M., Kahn, S. M., & Mewe, R. 2002, A&A, 392, 955

Vancura, O., Gorenstein, P., & Hughes, J. P. 1995, ApJ, 441, 680

Vink, J. 2008, Astronomy & Astrophyics, 486, 837

Vink, J., Laming, J. M., Kaastra, J. S., Bleeker, J. A. M., Bloemen, H., & Oberlack, U. 2001, ApJ, 560, L79

Vink, J., Laming, J. M., Gu, M.F., Rasmussen, A., & Kaastra, J.S. 2003, ApJ, 587, L31

Vink, J. 2012, Astronomy and Astrophysics Review, 20, 49

Wallerstein, G., Iben, I., Jr., Parker, P., et al. 1997, Reviews of Modern Physics, 69, 995

Warren, D. C., & Blondin, J. M. 2013, MNRAS, 429, 3099

Warren, J. S., & Hughes, J. P. 2004, ApJ, 608, 261

Warren, J. S., Hughes, J. P., Badenes, C., et al. 2005, ApJ, 634, 376

Williams, B. J., Blair, W. P., Blondin, J. M., et al. 2011, ApJ, 741, 96

Williams, B. J., Borkowski, K. J., Reynolds, S. P., et al. 2012, ApJ, 755, 3

Willingale, R., Bleeker, J. A. M., van der Heyden, K. J., Kaastra J. S., & Vink., J. 2003, A&A, 381, 1039

Woosley, S. E., & Heger, A. 2007, Phys. Rep., 442, 269

Woosley, S. E., & Weaver, T. A. 1995, ApJSS, 101, 181

Woosley, S. E., Heger, A., & Weaver, T. A. 2002, Reviews of Modern Physics, 74, 1015

Woosley, S. E., Wunsch, S., & Kuhlen, M. 2004, ApJ, 607, 921

Wu, C.-C., Leventhal, M., Sarazin, C.L., & Gull, T.R, 1983, ApJ, 269, L5

Xu, J.-L., Wang, J.-J., & Miller, M. 2011, Research in Astronomy and Astrophysics, 11, 537

Yamaguchi, H., Koyama, K., Katsuda, S., et al. 2008, PASJ, 60, 141

Yamaguchi, H., Tanaka, M., Maeda, K., et al. 2012, ApJ, 749, 137

Yamaguchi, H., Eriksen, K. A., Badenes, C., et al. 2014, ApJ, 780, 136

Yamaguchi, H., Badenes, C., Petre, R. et al. 2014, ApJ, 785, L27

Yang, X. J., Tsunemi, H., Lu, F. J., & Chen, L. 2009, ApJ, 692, 894

Yang, X. J., Tsunemi, H., Lu, F. J., et al. 2013, ApJ, 766, 44

Yatsu, Y., Kawai, N., Kataoka, J., Kotani, T., Tamura, K., & Brinkmann, W. 2005, ApJ, 631, 312